Journal of Energy Storage 140 (2025) 119113

Contents lists available at ScienceDirect

Journal of Energy Storage

journal homepage: www.elsevier.com/locate/est

Research papers

Degradation path indicators for lithium-ion batteries

S. Ramasubramanian [a], C. Plank [a,b], M.A. Danzer [a,b], F. Röder [a,*]

[a] University of Bayreuth, Bavarian Centre for Battery Technology (BayBatt), Weiherstraße 26, 95448, Bayreuth, Germany
[b] University of Bayreuth, Chair of Electrical Energy Systems, Universitätsstraße 30, 95447, Bayreuth, Germany

ARTICLE INFO

Dataset link: https://doi.org/10.5281/zenodo.15755725

Keywords:
Path-dependency
Degradation pathways
Unsupervised learning
Distribution of relaxation times analysis

ABSTRACT

Battery aging can follow multiple degradation pathways, which influence future aging due to self-amplification, self-limitation, and interactions among mechanisms. This phenomenon is known as path-dependent aging. Understanding path dependency is crucial for reliable lifetime prediction and requires identifying distinct degradation pathways. In this study, *k*-means clustering is applied to aging data from 48 commercial lithium-ion batteries (LIB), cycled under 24 combinations of temperature and C-rate. Key degradation metrics, including capacity fade, pulse resistance, and degradation modes, are used to construct path-indicator spaces. Clustering with degradation modes reveals three distinct degradation regimes, characterized by proximity in both path-indicator and stress-factor space. These regimes are further validated using microscopic analysis of the negative electrode and distribution of relaxation times analysis. Based on the findings, general guidelines are proposed for designing dynamic usage schedules to test path dependency in LIB aging. Therefore, the methodology presented in this study provides a generalizable framework for characterizing battery degradation with a multi-dimensional feature space and introduces an unsupervised approach for identifying distinct degradation pathways. Additionally, the proposed method can help in building dynamic test protocols that trigger distinct degradation pathways and aid in the development and validation of lifetime prediction models.

1. Introduction

During operation, lithium-ion batteries (LIB) can be exposed to a wide range of stress conditions [1–3], which can lead to a complex dependence of their degradation on the usage schedule, making it difficult to predict the lifetime of the battery. The complexity arises from multiple degradation processes and their interaction [4]. This can cause the LIB to follow different degradation paths in a latent degradation space, often described as the path dependency (PD) of battery aging [5].

In our previous work, we have classified PD into three levels based on whether the trajectory of the state of health (SOH) is affected by the operating conditions (PD I), the sequence of operating conditions (PD II), and whether there is an influence of the sequence on future trajectories (PD III). The emphasis is placed on the development of test protocols that can be used to investigate PD I-III in a laboratory setting, which is a key requirement for the development and parameterization of aging models that can make accurate predictions under realistic operating conditions [5]. An accurate prediction of battery lifetime can help in fault diagnosis of batteries [6]. and also the optimal design of batteries for different applications [7]. Understanding PD can also play an important role in managing batteries in their second-life applications [8] and can add to the existing knowledge base of battery recycling technologies [9].

Typically, PD I can be demonstrated by selecting static test conditions from a multidimensional stress-factor space (SFS), that can include depth of discharge (DOD), temperature, C-rate, etc., and analyzing the differences in the trajectory of the SOH [10–13]. It is well-known that LIBs can undergo different aging mechanisms under different stress conditions. For example, SEI growth is more significant at high temperatures [14,15], particle cracking at high C-rates [16], and lithium plating at low temperatures and high C-rates [17,18]. However, multiple mechanisms may be active under the same conditions, or the same degradation mechanism may vary in intensity depending on the applied stress. Both make it difficult to identify regions in the SFS that trigger a particular set of degradation mechanisms, i.e., a different degradation path.

Demonstration of PD II requires a test protocol in which the operating conditions are varied sequentially. PD II is expected if each of the selected conditions triggers a different degradation mechanism and if these degradation mechanisms interact with each other [5]. Due to sequential variation of the operating conditions, the number

* Corresponding author.
E-mail addresses: srivatsan.ramasubramanian@uni-bayreuth.de (S. Ramasubramanian), christian.plank@uni-bayreuth.de (C. Plank), danzer@uni-bayreuth.de (M.A. Danzer), fridolin.roeder@uni-bayreuth.de (F. Röder).

https://doi.org/10.1016/j.est.2025.119113
Received 10 July 2025; Received in revised form 2 October 2025; Accepted 20 October 2025
Available online 27 October 2025

of possible aging tests increases significantly compared to aging under static conditions. Since the dominant degradation mechanisms at a given test condition are usually not known in advance, a comprehensive PD II test consisting of all possible test sequences can be very resource intensive and time consuming.

Several studies have demonstrated PD II by applying calendar and cyclic aging to cells with similar cumulative aging conditions but different sequences [19,20]. PD II has also been demonstrated for cyclic aging alone, where only ambient temperature and C-rate was changed. For example, Liu et al. performed two studies where they cycled one group of cells at low temperature (−10 °C) followed by high temperature (50 °C) [21] (group A) and another group of cells were cycled first at high temperature followed by low temperature [22] (group B). The temperature change was carried out at an SOH of 80%–90% and cells were cycled to an SOH of 70%. They observed that plated lithium still present from the low temperature cycling can accelerate SEI growth. They found that the aging of the cells in group B was slower compared to the cells cycled at a constant temperature of 50 °C or −10 °C. As a result, they demonstrated PD in a simple cyclic aging experiment and, through extensive postmortem analysis, found complex interactions between SEI growth and plating that leads to electrolyte consumption. Although the presented studies provide valuable insight into PD, the choice of stress conditions and switching criterion is often arbitrary and does not involve a detailed understanding of the degradation pathways. Furthermore, it also has been shown that PD II is not always present but may depend on the magnitude of the applied stress, e.g. the C-rate [19]. Finally, understanding of path-dependency will also become increasingly important with the impending rise of batteries consisting of novel materials such as Silicon [23,24], whose degradation pathways are under intensive research [25]. In conclusion, it is important to have a detailed understanding of the possible degradation pathways in order to design tailored PD II studies.

One possibility to identify differences in degradation pathways is a detailed postmortem analysis. Although there are several methods available for this purpose, such as X-ray Photon Spectroscopy (XPS), Fourier Transform Infrared Spectroscopy (FTIR), Nuclear Magnetic Resonance (NMR), etc., they are often destructive, performed on a small number of samples, and resource intensive [26–28]. In addition, they are not suitable for implementation in battery management systems and thermal management systems, where information on degradation pathways can be useful to optimize battery operation.

An alternative non-destructive method to identify degradation pathways is degradation mode analysis [20,29,30]. As the cell ages, this method can be used to identify the loss of active material from the positive and negative electrodes (LAM_{pe}, LAM_{ne}) and the loss of cyclable lithium inventory (LLI), providing a more detailed insight into cell degradation. However, degradation modes are often correlated and do not directly indicate the underlying mechanisms. For example, if an active material lost due to particle fracture contained lithium, this aging process could lead to both LLI and LAM_{ne} or LAM_{pe} [31]. SEI growth or lithium plating that results in LLI can also cause LAM_{ne} by clogging pores or consuming electrolyte [4,32]. In addition, LLI can result from any type of side reaction, such as SEI growth and lithium plating, and these cannot be separated by the absolute value of LLI [33]. However, the relationship between applied stress conditions and the triggered degradation mechanisms is rarely analyzed in detail beyond the identification of dominant degradation modes [29,34]. This knowledge could be also be useful to reduce experimental load of designing thermal management systems [35].

Zhang et al. proposed the use of resistance increase vs. capacity decrease plots to separate capacitance loss due to lithium plating from capacity loss due to SEI growth [36]. By analyzing aging data from long-term measurements, they identify a clear line separating the two mechanisms based on the slope of the different curves in the plot. However, their method requires a hand-drawn line of separation and a long-term cycle to see a clear trend. Similarly, Bauer et al. used a 2D plot of capacity and power fade to separate high- and low-temperature aging processes using the sensitivity of pulse resistance values to capacity loss [37]. They emphasized that the representation of SOH in a multidimensional space can be useful in discriminating high- and low-temperature aging mechanisms in SFS.

In addition, dynamic electrochemical characterization methods such as electrochemical impedance spectroscopy [38,39] (EIS) and nonlinear frequency response analysis (NFRA) [40,41] have also been used to identify different degradation mechanisms.

In this work, we propose the design of PD II tests in which the individual operating conditions within a sequence are selected based on the degradation pathways identified from the aging data of PD I tests. As a result, the degradation pathways triggered by a PD II test protocol are no longer arbitrary, and the demand for PD II studies can be reduced. It has been suggested that a combination of features is essential for non-destructive identification and separation of mechanisms such as lithium plating and SEI growth [42]. Therefore, various degradation metrics such as capacity, pulse resistance and degradation modes are taken into consideration. Short-term aging tests are performed on 48 cells at different temperatures and C-rates. *k*-means clustering [43], an unsupervised learning algorithm, is used to identify clusters in the PIS that can be mapped to regions in the SFS, here C-rate and temperature. The identified degradation pathways are verified by postmortem analysis of the electrode under an optical microscope and DRT analysis of the impedance spectra of the cells. Finally, this information is used to provide general guidelines for the construction of PD II test protocols during cyclic aging. The overall workflow for this is summarized in Fig. 1.

2. Experimental details

2.1. Test cells

Commercially available lithium ion cells, CP1654 from Varta were used for this study. These cells utilize a graphite negative electrode and an NMC based positive electrode and has a nominal capacity of 120 mAh. The cell can be cycled between 3 V and 4.2 V and can be charged with a maximum C-rate of upto 2 C. An initial characterization of 180 cells from the batch was performed to determine distribution of cell capacity. The capacity after a CCCV discharge step was measured with a discharge C-rate of 0.5 C to 3 V and a cutoff discharge current of 0.02 C at 25 °C. It was found to be 124 mAh ± 2 mAh. The C-Rate throughout this study was calculated using a mean capacity of 124 mAh. 48 cells from this batch were tested at 24 different combinations of C-rate and temperature, while two cells were used for each condition.

2.2. Equipment

BaSyTec Cell Test Systems (CTS-Lab) are used for cyclic aging and reference performance tests (RPT). Two climate chambers (Binder KB53 and CTS T-40/50) were used to control environmental conditions. EIS and NFRA measurements are performed using Zahner ZENNIUM Pro. For opening the cells, a GS MEGA glovebox was used and a Keyence VHX-7000 microscope was used to perform the optical characterization.

2.3. Reference performance test

All cells are completely discharged to 3 V at the start of the reference performance test (RPT) and the ambient temperature is set to 25 °C. The cell is equilibrated at this temperature for 3 h. Here, 25 °C is used as a standard reference temperature at which the state of health of the cells before and after they undergo different degradation pathways can be analyzed. It is assumed that at 25 °C the reference performance test will have a minimal impact on the aging trajectory of the cell.

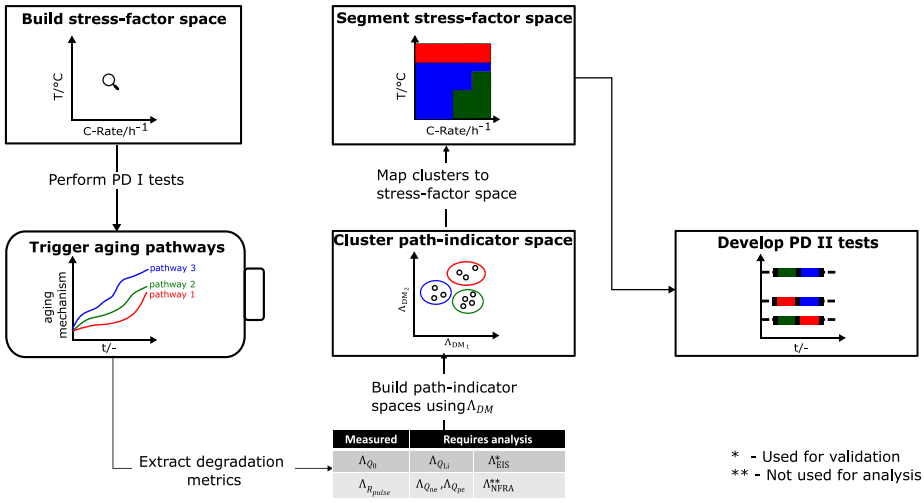

Fig. 1. Schematic of the process used to build PD II test protocols.

To calculate the cell capacity, the cell is cycled with a constant current (CC) charge C-rate of 0.5 C until a voltage of 4.2 V and a constant voltage (CV) is maintained until the current falls below 0.02 C. After a 10 min pause, the cell is discharged with a CC discharge with 0.5 C until it reaches 3 V followed by CV discharge at 3 V until the discharge C-rate rises above 0.02 C. A CC-CV discharge step is used to measure the overall capacity of the cell.

A pseudo-OCV (p-OCV) measurement is performed to identify the OCV characteristics of the cell. The cell is charged with a constant C-rate of 0.05 C until 4.2 V and after a rest of 10 min, discharged until 3 V with constant discharge C-rate of 0.05 C. Generally, p-OCV measurements are based on the assumption that the internal resistances of the cell have a minimal impact on the measured voltage if the applied current is sufficiently low and therefore, this value can be assumed to be the OCV. The choice of C-rates (0.05 C) is lower than some other p-OCV measurements found in literature 0.1 C [12]. Therefore, it is assumed that our choice of C-rate is sufficient to make the assumption. The p-OCV is used to calculate degradation modes.

The DC pulse resistance of each cell is measured by first charging it to 50% SOC based on the current capacity value, followed by a 2-h rest period. Then, a 1 C charge pulse is applied for 10 s, followed by a 2-h rest period. After this, a 1 C discharge pulse is applied for 10 s, followed by a 2-h rest period. Note that, in contrast to the other parts of the RPT, the C-rate of the pulse is adjusted based on the measured value of the capacity.

After the DC pulse resistance test, both EIS and NFRA measurements are performed on the cell at a temperature of 25 °C. EIS is performed with an amplitude of 0.05 C between 10 mHz and 100 kHz with 10 points per each decade of frequency. NFRA measurement is made between 10 mHz and 10 kHz with 5 points per each decade of frequency with an amplitude of 1.5 C. It is noted that NFRA data is not analyzed in this work, but can be found in the attached data set [44]. The amplitude of 0.05 C for the EIS measurement was empirically chosen in order to have a low enough amplitude that will not violate the linear and time-invariant assumptions. It is also usually a recommended value for LIBs and offers a good signal-to-noise ratio during the measurement [45].

50% SOC was chosen as the reference state at which the dynamic tests such as pulse resistance, EIS, and NFRA were performed. This is usually common practice in several aging studies that ensures that salient information about the kinetics of the cell as it ages can be identified while also optimizing the time taken for the reference performance tests [12,19]. Additionally, cells are expected to undergo very little aging at 50% SOC, which helps to reduce the impact of RPTs on the overall aging process [46].

2.4. Aging tests

A total of six temperatures (0 °C, 10 °C, 25 °C, 30 °C, 45 °C and 55 °C) and 4 C-rates (0.5 C, 0.75 C, 1 C, and 1.5 C) were used in this study. All the cells were aged using a constant-frequency cycle method to make efficient use of the available climate chambers and test channels.

At the beginning of the aging study, the cell was discharged to 3 V and the temperature of the climate chamber was set to the necessary value. The cell is then equilibrated at this temperature for 3 h.

The first and last cycles of the aging study involved a CC charge step at the chosen C-rate and temperature until the cell reaches 4.2 V and a CV step until the cell current falls below 0.02 C, after which the cell is immediately discharged at a C-rate of 0.05 C until it reaches the lower cutoff voltage.

All other aging cycles, start with a CC charge step at the given C-rate until the voltage of the cell reaches 4.2 V, which is followed by a CV step until the current falls below 0.02 C. After a 5 min pause, the cell is discharged with CC discharge step at the chosen C-rate until the voltage reaches 3 V. At the end of discharge, the cell is left in rest conditions until 5 h have passed since the cycle started. This is to ensure that cells at different C-rates spend same amount of time within the climate chamber. Further, this has the advantage that cycle number and aging time is directly coupled. The aging test is stopped after all cells have undergone 70 cycles, which corresponds to approximately 17 d.

It should be noted that 70 cycles represents a relatively short duration of cycling in comparison to typical aging measurements. However, this is in line with the objectives of this study, which was to get an early insight into the different degradation pathways of the cell at the chosen aging conditions and use it to design dynamic tests that trigger PD II. A cyclic aging phase of 70 cycles or approximately 17 days is assumed to be sufficient to capture the early-stage aging trends. It is possible that the choice of the cycling time for this study impacts the separability of the degradation pathways, i.e, a longer study could lead to identification of more pathways in the aging data.

The voltage limits for this cell was taken from the datasheet of the cell used in the study that has a graphite anode and an NMC based cathode. The C-rate is calculated using the average BOL capacity calculated in Section 2.1.

2.5. Post-mortem analysis

At the end of the aging tests, some cells from the group are selected and discharged with a C-rate of C/50 to 3 V, followed by a CV step at 3 V for 12 h. One cell that did not undergo any cycling is opened as a

reference cell with which the cells aged at other aging pathways can be compared. The choice of the cell from the aging study was dictated by the degradation pathways identified by the method proposed in this study. The rationale for this selection is discussed in detail in Section 4.4.

The cells are then opened inside a glovebox and the negative electrode is separated from the separators and positive electrode. The electrodes were stored within an inert atmosphere until they were used for microscopy under ambient conditions. In this study, the entire electrode was imaged under the microscope by separating the anode into 7–8 thin strips of electrode, which are placed between two glass slides.

An overview image of the electrodes is taken at a magnification of 20x followed by a detailed characterization of each part of the electrode at a magnification of 200x.

2.6. Analysis software

All of the plots in this work were made using Python version 3.12.2. The OCV fits were performed using scipy version 1.13.1. and the least squares function was used.

The code of the distribution of relaxation times analysis is part of the ec-idea software toolbox developed at the Chair of Electrical Energy Systems at the University of Bayreuth and is available online at https://www.ees.uni-bayreuth.de/en/ec-idea/index.html. *k*-means clustering [43] was performed using the sklearn package of version 1.5.1.

3. Analysis methods

3.1. Calculation of cell capacity

The cell capacity, Q_0 is calculated as the total discharge capacity during the discharge step of the reference performance test. This is the sum of the total capacity after CC discharge of the cell up to 3 V and the CV discharge at 3 V until the C-rate relaxes to a discharge C-rate of 0.02 C.

3.2. Calculation of DC pulse resistance

The pulse resistance is calculated from both the charge and discharge pulse at 50% SOC using Eq. (1).

$$R_{\text{pulse}} = \left| \frac{U(t = 10\ \text{s}) - U(t = 0\ \text{s})}{I_{\text{dc}}} \right| \tag{1}$$

In this equation, $U(t = 0\ \text{s})$ represents the cell voltage before the pulse, which is under open circuit conditions, at 50% SOC. $U(t = 10\ \text{s})$ represents the voltage at the end of the 10 s pulse and I_{dc} represents the applied current pulse of −1 C or 1 C.

3.3. Degradation mode analysis

Degradation mode analysis is performed using the method as presented by Schmitt et al. [29]. The charge step of the p-OCV test is used for the fitting and the voltage measured during the charge is given as E_0. The estimated full cell open circuit voltage $E_{0,\text{est}}$ is given by

$$E_{0,\text{est}}(\text{SOC}) = E_{0,\text{pe}}(\text{SOC}_{\text{pe}}) - E_{0,\text{ne}}(\text{SOC}_{\text{ne}}) \tag{2}$$

$E_{0,\text{pe}}$ refers to the open circuit potential (OCP) of the positive electrode as a function of its electrode-level SOC, SOC_{pe}. $E_{0,\text{ne}}$ refers to the OCP of the negative electrode as a function of its electrode-level SOC, SOC_{ne}. The OCP of the NMC622 cathode and graphite anode were taken from Chaouachi et al. [47]. The information was gathered using the notebook provided by the github repository of liiondb [48]. The discrete data for the electrodes was sampled at 1000 points between 0 and 1 using a linear interpolation and a cubic spline interpolant of this sampled data is used during the fitting.

The SOCs of the full cell and the SOCs of the electrodes for the positive and negative electrode are related according to

$$\text{SOC} = \alpha_{\text{pe}} \cdot (1 - \text{SOC}_{\text{pe}}) + \beta_{\text{pe}} \tag{3}$$

for the positive electrode and

$$\text{SOC} = \alpha_{\text{ne}} \cdot \text{SOC}_{\text{ne}} + \beta_{\text{ne}} \tag{4}$$

for the negative electrode, where α_{pe} and α_{ne} are the respective scaling factors by which the electrode OCPs are stretched and β_{pe} and β_{ne} are the respective shift factors by which the electrode OCPs are shifted.

The least squares algorithm is used to minimize the error between $E_{0,\text{est}}(\text{SOC})$ estimated by Eq. (2) and $E_{0,\text{mess}}(\text{SOC})$ from the measurement. The three tolerance parameters that track the change of independent variables, change of the cost function, and norm of the gradient were set to 10^{-12} and the scale of the variables is iteratively updated using the inverse norms of the columns of the Jacobian matrix.

After the fitting procedure is complete, the degradation modes can be estimated using Eq. (5), Eq. (6), and Eq. (7),

$$Q_{\text{Li}} = (\alpha_{\text{pe}} + \beta_{\text{pe}} - \beta_{\text{ne}}) \cdot Q_{\text{act}} \tag{5}$$

$$Q_{\text{pe}} = \alpha_{\text{pe}} \cdot Q_{\text{act}} \tag{6}$$

$$Q_{\text{ne}} = \alpha_{\text{ne}} \cdot Q_{\text{act}} \tag{7}$$

where, Q_{Li} is the total lithium inventory, Q_{ne} and Q_{pe} are the negative electrode and positive electrode capacity, respectively. Here, Q_{act} represents the capacity measured during the charge step of the p-OCV test.

For the fit performed on the cell after the RPT at Beginning-of-life (BOL), the scaling factors are bound between 1 and 2 and the shift factors are bound between −1 and 0. In this model, the shift factors are always negative as the electrode curves during the fit are shifted to the left so that they always have their origin at or below a full cell SOC of 0%. The scaling factors, α_{PE} and α_{NE} always have to be greater than 1 as the capacity of the full cell cannot be higher than the capacity of the individual electrodes.

When the fit is performed on the cell after the RPT at end-of-life (EOL), the upper limit of the scaling parameters α_{PE} and α_{NE} was adjusted such that the electrode capacities at the EOL is always lesser than or equal to the electrode capacities at the BOL. The upper bound of the scaling parameters for the EOL fits is calculated using

$$\alpha_{\text{i,EOL}_{\text{ub}}} = \alpha_{\text{i,BOL}_{\text{ub}}} \cdot \frac{Q_{\text{act,BOL}}}{Q_{\text{act,EOL}}}; i = [\text{PE}, \text{NE}] \tag{8}$$

in which $Q_{\text{act,BOL}}$ and $Q_{\text{act,EOL}}$ represent the capacity measured in the charge step of the p-OCV measurement at BOL and EOL, respectively. The average root mean square error (RMSE) between the estimated and measured OCV for all cells in this study at both BOL and EOL was less than 6 mV.

3.4. DRT analysis

Prior to the DRT analysis, the impedance data is validated against the criteria of linearity, stationarity, and time invariance (LTI) using two state-of-the-art methods: the extended Kramers–Kronig test [49], which relies on the Kramers–Kronig relation, and the Z-HIT algorithm [50,51], which utilizes the Hilbert transform applied to two-pole systems. Both techniques identify violations of these criteria by analyzing statistical errors (noise) and systematic errors (mean) of the residuals. The DRT analysis is classified as an inversion problem that transforms frequency domain data into the τ-domain. It is

mathematically defined as a Fredholm integral of the first kind [50]:

$$Z(j\omega) = R_0 + \int_{-\infty}^{\infty} \frac{h_{\mathrm{RC}}(\tau)}{1 + j\omega\tau} \mathrm{d}\ln\tau, \tag{9}$$

The deconvolution of the impedance data is performed in accordance with the procedure shown in [52]. It is based on the generalized DRT method introduced by Danzer [53], in which the integral equation is discretized and three additional serial lumped elements (R_0, C_0, and L_0) are included. Here, the second distribution function required to represent resistive-inductive characteristics is replaced by a single distribution function without applying a non-negativity constraint on its values. This allows for the modeling of arbitrary impedance spectra containing resistive-inductive effects:

$$Z(j\omega) = R_0 + j\omega L_0 + \frac{1}{j\omega C_0} + \sum_{k=1}^{N_\tau} \frac{h_{\mathrm{RC},k}}{1 + j\omega\tau_k}, \qquad h_{\mathrm{RC},k} \in \mathbb{R}. \tag{10}$$

This yields a system of linear equations that needs to be solved to obtain the discrete solution h_{RC} with N_τ elements for the distribution function. To get a meaningful and interpretable solution, a regularization technique must be employed. Here, the Tikhonov regularization (L2-norm) with a single regularization parameter λ is used. The regularization parameter is determined using the L-curve method [50,54]. In order to enable a more accurate comparison of the distribution functions of a heterogeneous data set, it is preferable to apply a fixed regularization parameter to all measurements. This is because the impact of the regularization parameter on the shape of the distribution function is greater than the effect of various noise levels in different measurements. Thus, the selected regularization parameter is averaged over several samples of BOL and EOL measurements. It is set to be 0.1, which is within the empirically suggested range for lithium-ion batteries by Hahn et al. [55].

The analysis itself is performed in two stages: First, the full impedance spectrum is transformed using the gDRT method. It covers the complete spectrum, including the high frequency resistive-inductive region as well as the diffusive branch observable for low frequencies. Subsequently, Gaussian kernels with

$$h_{\mathrm{Peak},i}(\tau_k, H, W, X, S) = H \cdot e^{\left(-0.5\cdot\left(\frac{(\log_{10}(\tau_k)-X)(1-\mathrm{sign}[\log_{10}(\tau_k)-X]\cdot S)}{W}\right)^2\right)} \tag{11}$$

are used to fit the peaks within the distribution function to quantify their polarization and time constant [50]. Each peak is parameterized by the height H, the width W, the position X, and the skewness S. The number of peaks are determined by a peak detection algorithm based on the first and second derivative of the distribution function. The polarization of one single peak can be calculated by evaluating the sum of polarization at every discrete τ_k of the optimized Gaussian Kernel:

$$R_{\mathrm{peak},i} = \sum_{k=1}^{N_\tau} h_{\mathrm{peak},i}(\tau_k) \tag{12}$$

For this aging study, the mid-frequency resistive-capacitive processes (i.e. charge-transfer and SEI) are of interest, and therefore the peaks corresponding to inductive or diffusive effects are only shown for completeness, but are not used in the discussion.

3.5. Evaluation of degradation metrics

A summary of the investigated battery degradation metrics DM is provided in the following section:

- Cell capacity (Q_0)
- Pulse resistance ($R_{\mathrm{pulse,ch}}$, $R_{\mathrm{pulse,dch}}$)
- Lithium inventory (Q_{Li})
- Active material capacity of the positive electrode (Q_{pe})
- Active material capacity of the negative electrode (Q_{ne})

For all degradation metrics, the relative change Λ_{DM} is calculated as percentage change between BOL and EOL:

$$\Lambda_{\mathrm{DM}} = 100 \cdot \left(\frac{\mathrm{DM_{BOL}} - \mathrm{DM_{EOL}}}{\mathrm{DM_{BOL}}}\right) \tag{13}$$

In this equation, $\mathrm{DM_{BOL}}$ represents the battery degradation metric at the beginning of life (BOL) and $\mathrm{DM_{EOL}}$ represents battery degradation metric at the end of life (EOL), which for this study is defined after 70 cycles.

The arithmetic mean of the relative changes $\bar{\Lambda}_{\mathrm{DM}}$ are calculated as

$$\bar{\Lambda}_{\mathrm{DM}} = \frac{1}{N}\sum_{i=0}^{N} \Lambda_{\mathrm{DM},i} \tag{14}$$

It is noted that in our study, the sample size N per condition was two cells. This decision was made as a compromise between stress factor density and statistical robustness, as the objective of the study was to get a quick insight into the possible degradation pathways before proceeding to a long-term aging study. Given the limitation of available channels, priority was given to exploring more operating conditions with two cells to show that the trends are reproducible. Therefore, the Λ_{DM} was calculated from DM measured at several closely spaced points in the SFS. Additionally, both of the cells are always shown in the plots and a pchip interpolator is used to interpolate between the measured conditions [56] in order to show the visible trends in the data. Finally, the impact of cell-to-cell variation on aging has been shown to become more significant as the cell degrades more [57]. As this work mostly explores early trends in aging under different operating conditions, it is assumed that the trends seen in this work is primarily due to different degradation pathways, with minor contributions from cell-to-cell variation. An in-depth analysis of any kind of inhomogeneity in the aging caused due to cell-to-cell variation is out of the scope of this work as it would require a significantly more number of cells than 2.

3.6. k-means clustering

k-means clustering is an unsupervised learning algorithm that can be used to separate points in a Euclidean space [43]. The degradation metrics that can be extracted from electrochemical aging are represented by $\mathbf{X} = \{\vec{x}_1, \ldots, \vec{x}_n\}$, where $\vec{x}_i$ is a vector of the mean relative change of the considered degradation metrics in a d dimensional path-indicator space (PIS) $\mathcal{P}$ and n is the number of investigated stress conditions, i.e. combinations of temperature and C-rate.

Given a number of clusters k, the algorithm aims to identify these clusters in the PIS $\mathcal{P}$ such that

$$J = \sum_{i=1}^{k}\sum_{\vec{x}\in C_i} \|\vec{x} - \vec{\mu}_i\|^2 \tag{15}$$

is minimized. In Eq. (15), C_i represents a cluster i, the vector $\vec{x}$ represents points within the cluster, and $\vec{\mu}_i$ represents the centroid of the cluster i.

Each iteration of the algorithm consists of two steps:

1. Given k means $\{\vec{\mu}_1 \ldots \vec{\mu}_k\}$ a given point $\vec{x}$ is assigned to a cluster C_i depending on the lowest value of its Euclidean distance to the centroid of all the clusters.
2. The new center of each cluster C_i is calculated and the location of the centroids is updated.

This iterative process continues until the positions of the centroids do not change or the objective function given by Eq. (15) remains stable.

The choice of the number of clusters is identified using the silhouette score (SIL) [58]. This is calculated using a combination of two distance metrics. For each datapoint $\vec{x}_i \in C_i$, a distance metric $u(\vec{x}_i)$ can be defined by

$$u(\vec{x}_i) = \frac{1}{n_{C_i} - 1}\sum_{x_j \in C_i, i\neq j} d(\vec{x}_i, \vec{x}_j) \tag{16}$$

Here, n_{C_i} the number of clusters, $\vec{x}_i$ represents the chosen point for which the metric is calculated, $\vec{x}_j$ represents the other points in the cluster, and $d(\vec{x}_i, \vec{x}_j)$ represents the distance between the points. This metric represents a similarity of each point to the cluster it is assigned too.

The mean dissimilarity of a point to other points in the other clusters is defined by $v(\vec{x}_i)$ as

$$v(\vec{x}_i) = \min_{J \neq I} \frac{1}{|C_J|} \sum_{\vec{x}_j \in C_J} d(\vec{x}_i, \vec{x}_j) \tag{17}$$

This equation calculates the minimum distance of each point $\vec{x}_i$ in cluster C_i to all the points in the other clusters C_j. Finally, the silhouette score is calculated as

$$s(\vec{x}_i) = \frac{v(\vec{x}_i) - u(\vec{x}_i)}{\max\{u(\vec{x}_i), v(\vec{x}_i)\}}, \quad n_{C_I} > 1 \tag{18}$$

and is a value between −1 and 1. A value closer to 1 indicates a higher quality of clustering and a SIL close to −1 indicates poor clustering quality, while a score near 0 suggests significant overlap between clusters. As the number of clusters increases, each cluster becomes smaller, reducing the distance between points within the same cluster while also decreasing the distance to points in other clusters. Consequently, the SIL typically decreases with more clusters, helping to avoid an excessive number of clusters that lack physical meaning. In practice, a SIL above 0.5 is often considered indicative of well-separated and meaningful clusters [59–61].

In addition to the silhouette score, davies-bouldin index (DBI) [62] and calinski-harabasz score (CHI) [63] were used as extra metrics to demonstrate robustness of the clustering process.

DBI is a similarity metric that is measured between two clusters C_i and C_j in $\mathcal{P}$. This is defined by Eq. (19) and Eq. (20)

$$R_{i,j} = \frac{s_i + s_j}{d_{i,j}} \tag{19}$$

In Eq. (19), $R_{i,j}$ is a measure of similarity between two clusters, which is calculated using s_i and s_j, which represent the average distance between the centroid of the clusters and each of the points in the cluster. $d_{i,j}$ represents the distance between the centroids of clusters that are being compared.

The DBI is then defined as the average value of this metric and it is given by Eq. (20), where k represents the total number of clusters in $\mathcal{P}$.

$$DB = \frac{1}{k} \sum_{i=1}^{k} \max_{i \neq j} R_{i,j} \tag{20}$$

DBI quantifies the similarity between clusters, with values closer to 0 indicating better clustering quality. However, as the number of clusters increases, the size of individual clusters decreases, which can cause the numerator of Eq. (19) to approach zero. Consequently, relying on DBI alone may lead to formation of clusters that lack physical meaning. Therefore, DBI is employed here as a complementary metric alongside the SIL.

CHI can be described as the ratio of the dispersion between the different clusters in $\mathcal{P}$ and the dispersion within a given cluster C_i. A higher value of CHI indicates when the clusters are compact and clearly separated from each other. This is described by

$$CHI = \frac{tr(B_k)}{tr(W_k)} \times \frac{N_e - k}{k - 1} \tag{21}$$

In this equation, N_e represents the total number of points and k represents the number of clusters. $tr(B_k)$ represents the sum of the main diagonal values of the matrix representing dispersion between different clusters. $tr(W_k)$ represents the sum of the main diagonal values of the matrix representing dispersion within a given cluster C_i.

For CHI, as the size of the individual clusters become smaller, the dispersion within a given cluster reduces more than the dispersion between different clusters, which artificially inflates the value of CHI. As a result, using CHI alone as a metric of clustering might result in the formation of too many clusters that offer no insight. Therefore, this is used as a complementary metric to DBI and SIL in this work. The number of clusters is then selected using the following steps.

- A d dimensional PIS $\mathcal{P}$ is formed by choosing $\bar{\Lambda}_{\mathrm{DM}}$ extracted from aging data at the 24 tested conditions.
- The points in this space are clustered using the k-means algorithm, with the number of clusters n varied from 2 to 24. For each n, the corresponding SIL, DBI, and CHI are computed to assess the quality of the cluster. The clustering is also repeated using 300 random seeds to verify the stability of the predicted clusters.
- The values of n after which the average value of DBI shows a monotonic decrease or the average value of CHI shows a monotonic increase is then discarded.
- This study uses a heuristic that the optimal number of clusters should have a value of SIL greater than 0.5, a low value of DBI, and a high value of CHI.
- If at least two out of the three metrics predict a certain value of n as the optimal number of clusters for a majority of the random seeds, this value is selected for the cluster analysis.

The scikit-learn implementation of k-means clustering used in this work also uses the kmeans++ algorithm [64] to initialize the centroids, which is a smart initialization method that attempts to make the initial choice of cluster centers have maximum separation from each other. All of the other parameters, apart from two, are left at their default values. The parameter that decides the random number generation for centroid initialization was set to 269 for all the clustering done in this work. The random seed value of 269 was selected following an evaluation of the influence of different seeds on the stability of the predicted clusters. Clustering analysis was conducted using 300 distinct random seeds, and the corresponding SIL, DBI, and CHI metrics for various values of n are reported in Section 4.3.1. The chosen seed yielded the highest SIL value above 0.5 and optimal values for DBI or CHI.

4. Results and discussion

In the following, the trends in the relative change of the degradation metrics, that include directly measured quantities (Λ_{Q_0}, $\Lambda_{R_{pulse,ch}}$, $\Lambda_{R_{pulse,dch}}$) and metrics estimated via OCV fitting ($\Lambda_{Q_{Li}}$, $\Lambda_{Q_{ne}}$, $\Lambda_{Q_{pe}}$), are analyzed in Section 4.1. Section 4.2 presents an evaluation of EIS measurements, which provides insights into the impact of applied stress factors on different dynamic processes in the cell. Subsequently, two PISs are constructed, upon which k-means clustering is applied. These regimes are then mapped onto the corresponding regions in the SFS. Finally, the identified regions are examined in detail through microscopic imaging and distribution of relaxation times (DRT) analysis for validation. Based on these investigations, potential degradation mechanisms occurring in these regions are proposed.

4.1. Analysis of the degradation metrics

4.1.1. Capacity fade

Fig. 2a shows the temperature dependence (0 °C to 55 °C) of the capacity fade (Λ_{Q_0}) for cells cycled at different C-rates: 0.5 C (circles), 0.75 C (triangles), 1 C (squares), and 1.5 C (pluses). Each data point represents the result from one cell. A pchip interpolator is fitted to the mean values at each condition (from two cells) and is shown as colored lines, highlighting the overall trend of Λ_{Q_0} with temperature for each C-rate.

Λ_{Q_0} shows a minimum value of around 2% between 25 °C–30 °C at all C-Rates. It increases as the ambient temperature decreases below 25 °C, with a maximum average capacity fade of around 10% at 0 °C and 1 C. The Λ_{Q_0} also increases as the temperature increases, with a maximum average capacity fade of 4% at 55 °C and 0.5 C. This indicates

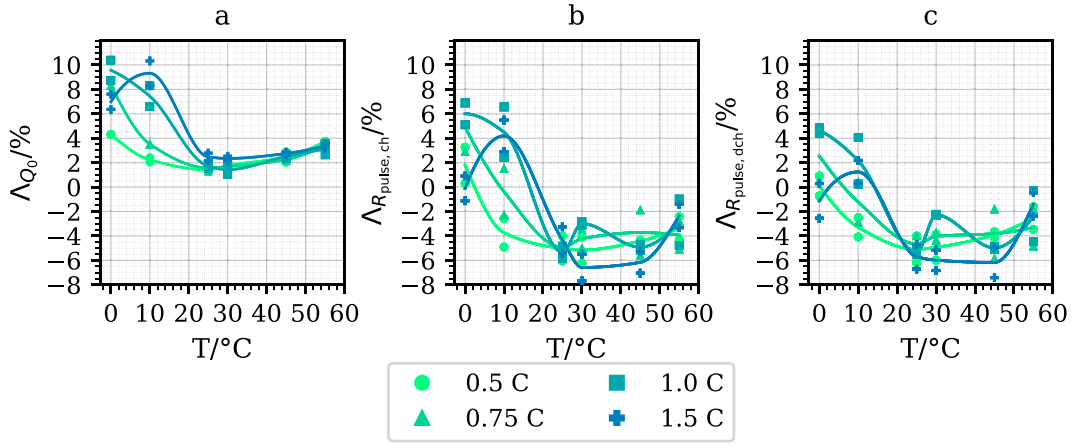

Fig. 2. Measured value of the degradation metrics, (a) Λ_{Q_0}, (b) $\Lambda_{R_{pulse,ch}}$, (c) $\Lambda_{R_{pulse,dch}}$ for different values of ambient temperatures (0 °C, 10 °C, 25 °C, 30 °C, 45 °C, 55 °C) plotted for 4 C-rates (0.5 C, 0.75 C, 1 C, and 1.5 C) shown by different shapes. The line passing through the points represent a pchip interpolator that is fit to the average measured values at each condition.

that the capacity fade increases above and below a temperature of 25 °C, but not in the same manner.

Λ_{Q_0} also shows a significant dependence on C-rates at low temperatures (T≤25 °C). At 10 °C, and 0.5 C it is around 2% and increases with increasing C-Rate until approx. 9% at 1 C. However, this trend changes at 0 °C for the highest C-rates. At a C-Rate of 1.5 at 0 °C it is only 7%, which is lower compared to 0.75 C and 1 C. C-Rate dependency is less distinct with increasing temperature. At the highest temperatures, no significant dependence is visible.

The asymmetrical trend in the magnitude of Λ_{Q_0} at low and high temperatures is generally expected to arise from the fact that different aging mechanisms are probably active at different temperatures, possibly lithium plating at low temperatures and SEI growth at high temperatures [65–67]. This hypothesis is further supported by the observed C-rate dependence at low temperatures. Lithium plating is expected to have a strong dependence on C-rate as higher C-rates could lead to a large electrolyte potential that could accelerate this side reaction [4,18,66]. On the other hand, SEI growth is a side reaction that occurs continuously in a battery and is accelerated at high temperatures, therefore, it is primarily dependent on temperature and time [4] with only a weak dependence on C-rate [67].

The rather counter-intuitive reduction in Λ_{Q_0} at 0 °C and 1.5 C has been previously reported in the literature and has been attributed to higher overpotentials in the CC phase of charging, which means the upper voltage limit is reached much before the graphite is fully lithiated. This leads to a longer CV phase, which allows reversibly plated lithium to reintercalate back into graphite [68,69].

In summary, the Λ_{Q_0} is higher at low temperatures (T≤25 °C) vs. high temperatures (T>25 °C) and the Λ_{Q_0} at low temperatures is more dependent on the C-rate than high temperatures. This inherent difference could be exploited to identify possible degradation pathways in the battery.

4.1.2. Change in pulse resistance

Fig. 2b and c shows the temperature dependence (0 °C to 55 °C) of the change in the pulse resistance calculated from the charge ($\Lambda_{R_{pulse,ch}}$)and discharge pulse ($\Lambda_{R_{pulse,dch}}$) at 50% SOC, for cells cycled at different C-rates: 0.5 C (circles), 0.75 C (triangles), 1 C (squares), and 1.5 C (pluses). Each data point represents the result from a single cell. A pchip interpolator is fitted to the mean values at each condition and is shown as colored lines, highlighting the overall trend of ($\Lambda_{R_{pulse,ch}}$) and ($\Lambda_{R_{pulse,dch}}$) with temperature for each C-rate. As all Λ_{DM}s in this study are calculated using Eq. (13), an increase in pulse resistance would result in a negative value of the relative change in pulse resistance. Therefore, the calculated values of $\Lambda_{R_{pulse,ch}}$ and $\Lambda_{R_{pulse,dch}}$ are multiplied with a −1 for the purpose of clarity.

The $\Lambda_{R_{pulse,ch}}$ has a maximum value of 6% at (0 °C, 1 C) and a minimum of approximately −6.5% at (30 °C, 1.5 C). Similarly, for the discharge pulse, the $\Lambda_{R_{pulse,dch}}$ reaches a maximum average value of 5% at (0 °C, 1 C) and a minimum of about −6.25% at (45 °C, 1.5 C). Despite these differences in magnitude, the values calculated from both the charge and discharge pulses exhibit similar trends with respect to temperature and C-rate. Therefore, the discussion in this paper will focus on the trend of the value calculated from the charge pulse.

The $\Lambda_{R_{pulse,ch}}$ becomes more positive as the temperature decreases below 25 °C. At 10 °C, it is a positive value greater than 4% only at 1 C and 1.5 C. At 0 °C, the value is positive for all of the measured C-rates. As the temperature increases above 25 °C, the change in pulse resistance at 1.5 C shows a minimum negative value of around -7% at 30 °C. For the other C-rates, it shows a minimum negative value of around -5% at 25 °C. The value also becomes less negative as the temperature increases above 30 °C for all C-rates. At 55 °C, the cell cycled at 1.5 C shows a value of around −2%. It can be seen that the pulse resistance can both increase and decrease as the cell degrades and the magnitude of this change shows a different and less obvious trend on temperature and C-rate as compared to $\bar{\Lambda}_{Q_0}$.

The difference between the pulse resistance calculated using the charge and discharge pulse have been previously reported in the literature [45,70,71], where it was suggested that discharge resistance at 50% SoC is typically higher than charge resistance. Barai et al. attributed this to the difficulty of pushing lithium ions from a lower potential anode to a higher potential cathode during a discharge pulse [45].

The complex dependence of the change in the pulse resistance with temperature and C-rate could arise from the fact that the pulse resistance of the cell is affected by degradation pathways that take place at both the anode and cathode, which may lead to an increase and decrease in the cell resistance at the same time. The final value of the measured change could indicate the dominant aging pathway.

Generally, pulse resistance is expected to show an overall increase during long-term aging studies [27,34]. At temperatures less than 10 °C and at higher C-rates, lithium plating is expected [4,18,66]. Rangarajan et al. reported that plating could lead to increase in resistances if the plated lithium consumes more electrolyte and forms secondary SEI [72]. Additionally, if the grown SEI electrically isolates the plated lithium, it might form dead lithium that could clog pores and further increase the resistance values [4,32]. Therefore, various

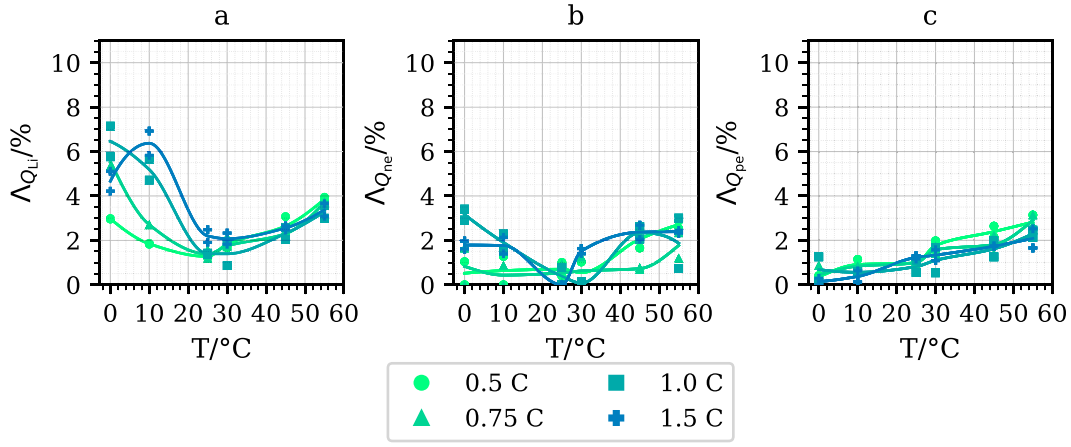

Fig. 3. Measured value of the degradation metrics, (a) $\Lambda_{Q_{Li}}$, (b) $\Lambda_{Q_{ne}}$, (c) $\Lambda_{Q_{pe}}$ for different values of ambient temperatures (0 °C,10 °C,25 °C,30 °C,45 °C,55 °C) plotted for 4 C-rates (0.5 C, 0.75 C,1 C, and 1.5 C) shown by different shapes. The line passing through the points represent a pchip interpolator that is fit to the average measured values at each condition.

degradation mechanisms can lead to the positive change in pulse resistance observed in the measurements at low temperatures.

As temperatures increase above 25 °C, SEI growth is expected to be the main cause of degradation. Typically, SEI growth is expected to increase the resistance of the cell as a thicker layer is expected to have a higher resistance for lithium-ions. Furthermore, SEI could also lead to electrolyte consumption and blockage of pores leading to an increase in pulse resistance [4]. Additionally, mechanisms at the Cathode such as microcracking could lead to internal pressure build up that could reduce the porosity of the electrodes [73]. However, in the measurements reported in this study, resistance decreases for all C-rates at temperatures greater than 25 °C.

Several studies have reported an initial reduction in pulse resistance during the so-called "break-in" cycles of the battery [12,74–77]. This reduction can be assigned to several mechanisms, such as an increase in the interfacial area of the electrodes, an improved wetting of the electrolyte, or improved electrical contact between the particles due to an internal build-up of pressure. For example, Rangarajan et al. suggest that lithium plating could lead to initial reduction in the resistance of the cell as the dendrites improve the interfacial area of the electrodes [72]. Furthermore, cracking of particles, which is usually a precursor to particle fracture, also leads to a reduction of resistances and can occur on both electrodes [73,75,76,78]. However, if SEI growth or particle cracking leads to internal pressure build-up, it could lead to better electrolyte wetting or contact between particles that leads to a reduction of resistances [74]. Any of the mechanisms discussed above could cause the reduction in resistance observed at higher temperatures.

In summary, the $\Lambda_{R_{pulse,ch}}$ at 0 °C is generally positive at all C-rates and at 10 °C, it is positive for 1 C and 1.5 C. It is negative at 10 °C for C-rate of 0.5 C and 0.75 C and negative for all C-rates at temperatures greater than 10 °C. Different degradation pathways could have competing impact on the pulse resistance, which could lead to this complex trend. This sensitivity of resistance values to the prevalent aging mechanisms could be exploited to identify possible degradation pathways in the battery.

4.1.3. Degradation modes

Fig. 3a, b, and c show the temperature dependence (0 °C to 55 °C) of the degradation modes, $\Lambda_{Q_{Li}}$, $\Lambda_{Q_{ne}}$, $\Lambda_{Q_{pe}}$, for cells cycled at different C-rates: 0.5 C (circles), 0.75 C (triangles), 1 C (squares), and 1.5 C (pluses). Each data point represents measurements from one cell. A pchip interpolator is fitted to the mean values at each condition and is shown as colored lines, highlighting the overall trend of the degradation modes with temperature for each C-rate.

The $\Lambda_{Q_{Li}}$ as shown in Fig. 3a has a minimum value of around 1.5% at a temperature of 25 °C for the C-rates 0.5 C, 0.75 C, and 1 C. For a C-rate of 1.5 C, a minimum value of around 2% is observed at a temperature of 30 °C. The $\Lambda_{Q_{Li}}$ increases as the temperature decreases below 25 °C, with a maximum value of 6.5% at 0 °C and 1 C. The $\Lambda_{Q_{Li}}$ also increases as the temperature increases above 25 °C, with a maximum value of 4% at 55 °C and 0.5 C. This indicates that, $\Lambda_{Q_{Li}}$ increases above and below a temperature of 25 °C but not in the same manner. In general, $\Lambda_{Q_{Li}}$ shows a similar trend as Λ_{Q_0}.

$\Lambda_{Q_{Li}}$ also shows a significant dependence on C-rates at low temperatures (T≤25 °C). At 10 °C, and 0.5 C it is around 2% but at 1.5 C, it is around 6.5%. However, at 0 °C and 1.5 C the value is lower with only 4.5%. It is noted that $\Lambda_{Q_{Li}}$ at this temperature range is lower than Λ_{Q_0} at low temperatures, which indicates that at lower temperatures there are possibly additional significant contributors that lead to Λ_{Q_0}.

The $\Lambda_{Q_{Li}}$ at 1.5 C shows a high value compared to the other C-rates at 25 °C and 30 °C. However, as the temperature increases further, no dependence is visible with the C-rate. Additionally, the $\Lambda_{Q_{Li}}$ is similar to Λ_{Q_0} at high temperatures, which indicates that $\Lambda_{Q_{Li}}$ is probably mostly responsible for Λ_{Q_0} in this temperature range.

The $\Lambda_{Q_{ne}}$ shown in Fig. 3b shows a minimum value of nearly 0% at a temperature of 30 °C for the C-rates 0.5 C, 0.75 C, and 1 C. For 1.5 C, it shows a value of nearly 0% at a temperature of 25 °C. The $\Lambda_{Q_{ne}}$ increases as the temperature decreases below 25 °C, shows a maximum value of 3% at 0 °C and 1 C. The $\Lambda_{Q_{ne}}$ also increases as the temperature increases above 25 °C, with a maximum value of 2.5% at 55 °C and 0.5 C. This indicates that, $\Lambda_{Q_{ne}}$ increases above and below a temperature of 25 °C in a similar manner.

$\Lambda_{Q_{ne}}$ also shows a dependence on C-rates at low temperatures (T≤10 °C). At 0 °C and 1 C it is around 3% and at 1.5 C it is around 2%, as compared to 0.5 C and 0.75 C, where it is around 0.5%. In contrast, as the temperature increases from 25 °C, only the $\Lambda_{Q_{ne}}$ at 30 °C and 1.5 C is higher compared to the values at the other C-rates. However, as the temperature increases further, no significant dependence is visible with the C-rate.

Finally, $\Lambda_{Q_{pe}}$ is shown in Fig. 3c, which has a minimum value of less than 1% at a temperature of 0 °C and the highest value of around 3% at around 55 °C. Generally, $\Lambda_{Q_{pe}}$ increases with temperature and does not show a significant and clear dependence on the C-rate.

$\Lambda_{Q_{Li}}$ indicates the lithium inventory that is lost during cycling. This effect is often assigned to side reactions such as SEI growth or lithium plating [4,32]. The asymmetry in $\Lambda_{Q_{Li}}$ at low (T≤10 °C) and

high temperatures (T≥25 °C) suggests different dominant mechanisms such as lithium plating at low temperatures and SEI growth at high temperatures [65–67]. This is supported by the stronger dependence on C-rate observed at low temperatures, which is consistent with lithium plating being more sensitive to C-rate [4,18,66], whereas SEI growth shows only a weak dependence on C-rate [67].

$\Lambda_{Q_{Li}}$ at T≤10 °C and at all C-rates was lower than Λ_{Q_0} but not at higher temperatures, which has previously been reported in other studies [12,79]. This could be an indicator that at low temperatures and high C-rates, plated Lithium is an active side reaction that leads to loss of lithium inventory. However, there are additional mechanisms that could take place. This hypothesis is further supported by looking at the dependence of $\Lambda_{Q_{ne}}$ on temperature.

At low temperatures and high C-rates, the graphite electrode is expected to be brittle, which could lead to disconnection of the particles. In addition, side reactions such as lithium plating could also block pores in electrodes or consume electrolyte [32,72], which could lead to the isolation of certain regions of the electrode. If lithiated particles become isolated, it could lead to LLI and if delithiated particles become isolated, it could lead to capacity fade and increased resistance [32]. It is possible that the difference between the capacity fade and LLI at low temperatures, mostly appears as LAMne. This phenomenon can be observed in the results of several other studies, but has never been analyzed in detail [12,79]. Koleti et al. suggest that lithium plating can lead to high levels of mechanical stress and that localized lithium plating could contribute to high loss of active material during the early stages of cyclic aging [80]. Ecker et al. showed that inhomogeneous nature of lithium plating could also lead to loss of active material in the negative electrode [18]

At high temperatures, a graphite electrode is expected to undergo high thermal stress, which can accelerate particle fracture during cycling. If this loss is due to parts of the graphite that are not used during cell operation, it might not immediately lead to a capacity-fade [4]. It is possible that temperature plays a larger role in this process than C-rate. However, no further conclusive statements can be made here without further analysis.

There is minimal LAMpe that increases with temperature, but it is unlikely to be a major contributor to capacity loss, as the percentage is mostly lower than the other degradation modes. At high temperatures, thermal stresses due to cycling could also lead to the formation of cracks in cathode particles that could lead to fracture. Furthermore, positive electrode structural change and decomposition is expected to be mainly exacerbated by high temperatures, but is not directly affected by C-rate [4]. This can explain the approximately linear dependence of $\Lambda_{Q_{pe}}$ in the measured data.

In summary, analysis of degradation modes indicates that $\Lambda_{Q_{Li}}$ closely follows the trend of Λ_{Q_0}, with clear differences in the magnitude at T≤ 10 °C and higher C-rates (1 C and 1.5 C), suggesting that side reactions and their consequences are the dominant aging mechanism under tested conditions. $\Lambda_{Q_{pe}}$ is unlikely to significantly impact the capacity fade due to its lower magnitude compared to the other degradation modes. In contrast, $\Lambda_{Q_{ne}}$ occurs at both extremes of temperature, with a stronger dependence on the C-rate at low temperatures than at high temperatures, further supporting the idea of distinct degradation pathways in these regions. Although definitive confirmation of these pathways requires a detailed postmortem analysis, the observed trends highlight interrelated degradation behavior that justifies the use of $\Lambda_{Q_{Li}}$, $\Lambda_{Q_{ne}}$, $\Lambda_{Q_{pe}}$ collectively to identify possible degradation pathways in the battery.

4.2. Electrochemical impedance spectroscopy

Fig. 4 illustrates the EIS spectra at BOL and EOL for all the cells aged at 0 °C (Fig. 4a–d) and 55 °C (Fig. 4e–h). The BOL measurement for the two cells at each condition is depicted with a black dashed line and EOL measurements are marked with black solid lines. Although the cells were aged at different temperatures, all EIS measurements were performed at 25 °C and 50% SOC. The BOL spectra of the cells that were aged at other conditions not discussed in the section are shown with light gray lines. It is noted that the spectra shown here are only the resistive-capacitive part of the impedance roughly identified between 1 Hz and 40 kHz. Three specific frequency points are marked in the Nyquist plots by a circle (10 Hz), triangle (1 kHz), square (16 kHz) for both the BOL and EOL measurements.

The presented EIS spectra appear as a depressed semicircle that can be divided into three regions. At frequencies greater than 16 kHz, the impedance spectra intersect with the real axis for both BOL and EOL measurements. The next region between 10 Hz to 16 kHz shows the rest of the flattened semicircle. For this cell, only a single semicircle is visible, which is likely caused by the overlap of several processes in the cell. At frequencies lower than 10 Hz, the flattened semicircle ends and only the beginning of the diffusive arc is visible, which arises from the fact that the low frequency part of the impedance was removed in order to only show the resistive-capacitve parts of the spectra.

The intersection with the real axis of the Nyquist plot varies between 0.17 Ω to 0.19 Ω. The intercept is the overall ohmic resistance of the cell, that arises as a result of the resistance of wires, current collectors, and electronic and ionic resistance of the electrodes and the electrolytes [53]. It can be seen that the ohmic resistance increases for all of the cells aged at 0 °C and at 55 °C and end up between 0.18 Ω to 0.20 Ω. This indicates that the degradation pathway at this temperatures and C-rates impact the electronic and ionic conductivities of the electrode, electrolyte or both.

The resistive-capacitive region between 1 Hz and 16 kHz is usually affected by processes such as transport through the SEI, electrochemical reactions at the two electrodes, or the charging of the double layer [78]. The arc of this semicircle seems to increase its diameter for the cells aged at 0 °C and decrease for cells aged at 55 °C as evident by the expansion of this part of the semicircle for the former and a clear reduction in size for the latter. This can be seen by the magnitude of the impedance at 10 Hz, which can be calculated from the real and imaginary parts of the impedance measured from the Nyquist plot. It is between 0.39 Ω to 0.40 Ω at BOL for the cells tested at the two temperatures. For the cells aged at 0 °C, this value increases to a maximum of 0.42 Ω at 1 C and for the cells tested at 55 °C, this value reduces to around 0.37 Ω at 0.75 C. At 0 °C, this value shows a minor C-rate dependence as the semicircle seems to expand until 1 C, before showing a less significant increase at 1.5 C. This indicates that processes such as ion transport through the SEI and charge transfer at the electrodes could be impacted by the degradation mechanisms that are active at the hot and cold temperatures [73,76,77].

To summarize, the applied stress factors lead to an increase in the ohmic resistances and to different effects on the impedance in the frequency range between 10 Hz and 1 kHz, i.e. an increase of the resistive-capacitive arc at low temperatures and a decrease at higher temperatures. In both cases, the effect is slightly enhanced by increasing the C-rate. It can be seen that EIS provides further information about different processes in the battery, which could be also useful to differentiate degradation pathways.

However, it is noted that in this section only a qualitative discussion of the trends is provided. Thus, it can be seen that impedance is affected differently by different aging conditions, but for a more detailed assessment further analysis is needed. In this work, we applied DRT analysis and use it to validate the degradation pathways identified using the PISs formed by the degradation metrics described in Section 4.1.

4.3. Clustering analysis of path-indicator space

In this section, a 2D PIS using $\bar{\Lambda}_{Q_0}$ and $\bar{\Lambda}_{R_{pulse,ch}}$ (PIS I) and a 3D PIS using $\bar{\Lambda}_{Q_{Li}}$, $\bar{\Lambda}_{Q_{pe}}$ and $\bar{\Lambda}_{Q_{ne}}$ (PIS II) is constructed by a k-means clustering based analysis. The three clustering metrics, SIL, DBI, and CHI are calculated for a number of clusters varying from 2 to 23. The

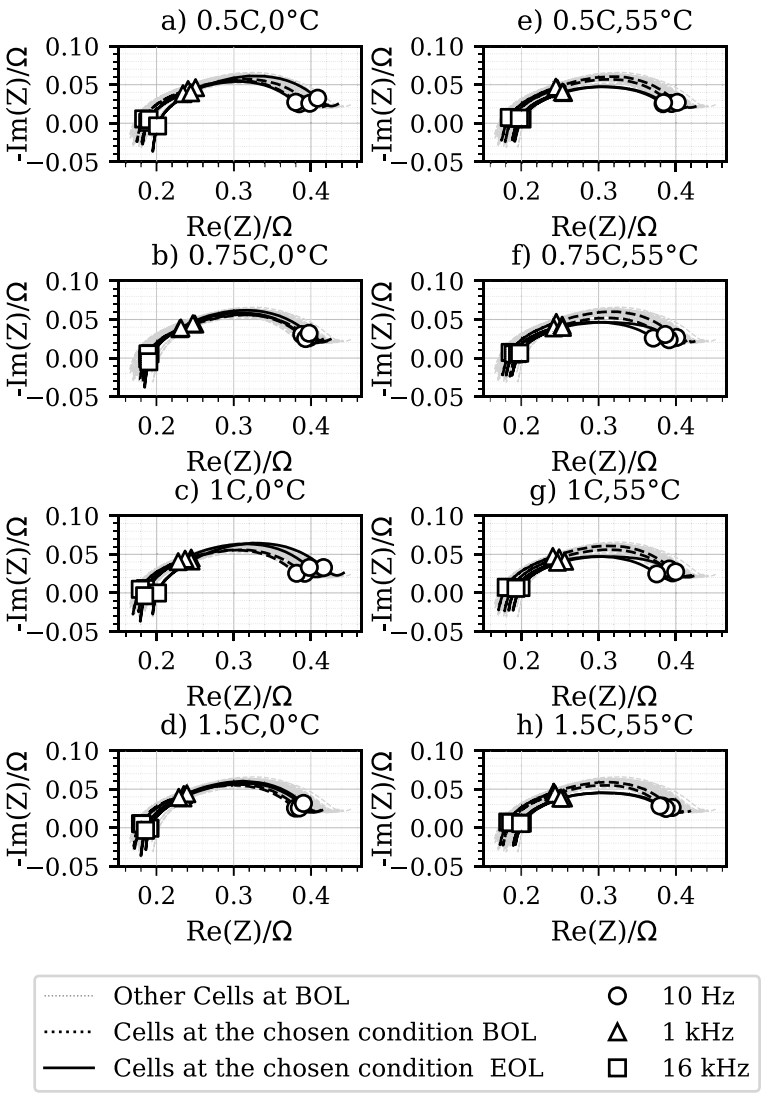

Fig. 4. EIS measurement at BOL for the cells at all conditions (light gray), selected BOL conditions are represented by a black dashed line and EOL (black solid line) at (a) 0 °C, 0.5 C, (b)0 °C, 0.75 C, (c)0 °C, 1 C, (d)0 °C, 1.5 C,(e) 55 °C, 0.5 C, (f)55 °C, 0.75 C, (g)55 °C, 1 C, (h)55 °C, 1.5 C.

first and second optimal number of clusters are identified using the method described in Section 3.6 and these results are reported. Finally, the points in these clusters are mapped to the SFS in order to verify whether it is a unique pathway in the cell that is triggered by a certain region of the SFS.

The metrics selected for PIS I were $\bar{\Lambda}_{Q_0}$ and $\bar{\Lambda}_{R_{pulse,ch}}$, as these DM's are typically straightforward to measure in the field. These two metrics are closely interrelated, and considering them together allows for a more comprehensive analysis of their interdependencies. In contrast, the metrics of PIS II $\bar{\Lambda}_{Q_{Li}}$, $\bar{\Lambda}_{Q_{pe}}$ and $\bar{\Lambda}_{Q_{ne}}$ (PIS II) are quantities derived using a fitting procedure and cannot be directly measured. Nevertheless, they enable the decomposition of degradation into electrode-specific contributions, which results in a deeper insight into the influence of operating conditions on the degradation pathways. It is also possible to implement the calculation of degradation modes in battery management systems [81]. Additionally, the selection of these metrics can be motivated by earlier works that employed them to separate aging mechanisms [36,37] or to discuss path-dependent aging [82].

It should be noted that the chosen degradation metrics represent only a subset of the many possible feature combinations for building a PIS. In theory, the dimensions of the PIS is not limited, and higher-dimensional spaces could capture additional information. While metrics derived from techniques such as EIS [83,84] or NFRA [85,86] could further enhance pathway separation, extracting physically meaningful features from this data is beyond the scope of this study and will be pursued in future work. The present work therefore focuses on features that are both physically motivated and experimentally accessible. Nevertheless, the EIS and NFRA data is provided to the wider community in the attached dataset [44]

4.3.1. Optimal number of clusters for PIS I and II

Prior to performing cluster analysis, the optimal number of clusters for the two spaces has to be chosen. This is done using the method described in Section 3.6. After the analysis, the mean value of each of the metrics SIL (dark blue), DBI (light blue), and CHI (green) after 300 runs are shown as a bar graph in Fig. 5a for PIS I and Fig. 5c for PIS II. Individual points contributing to this mean is overlaid as a scatter plot along with the error bar for each of the metrics. The value of the metric for the random seed 269, which is used in this study is also shown by black triangles. The optimal cluster number n chosen based on the heuristics described in Section 3.6 for each of the 300 runs is summarized as a bar graph in Fig. 5b for PIS I and Fig. 5d for PIS II. For both the PISs it was identified that a cluster number $n > 4$ either resulted in SIL values less than 0.5 or resulted in the DBI monotonically

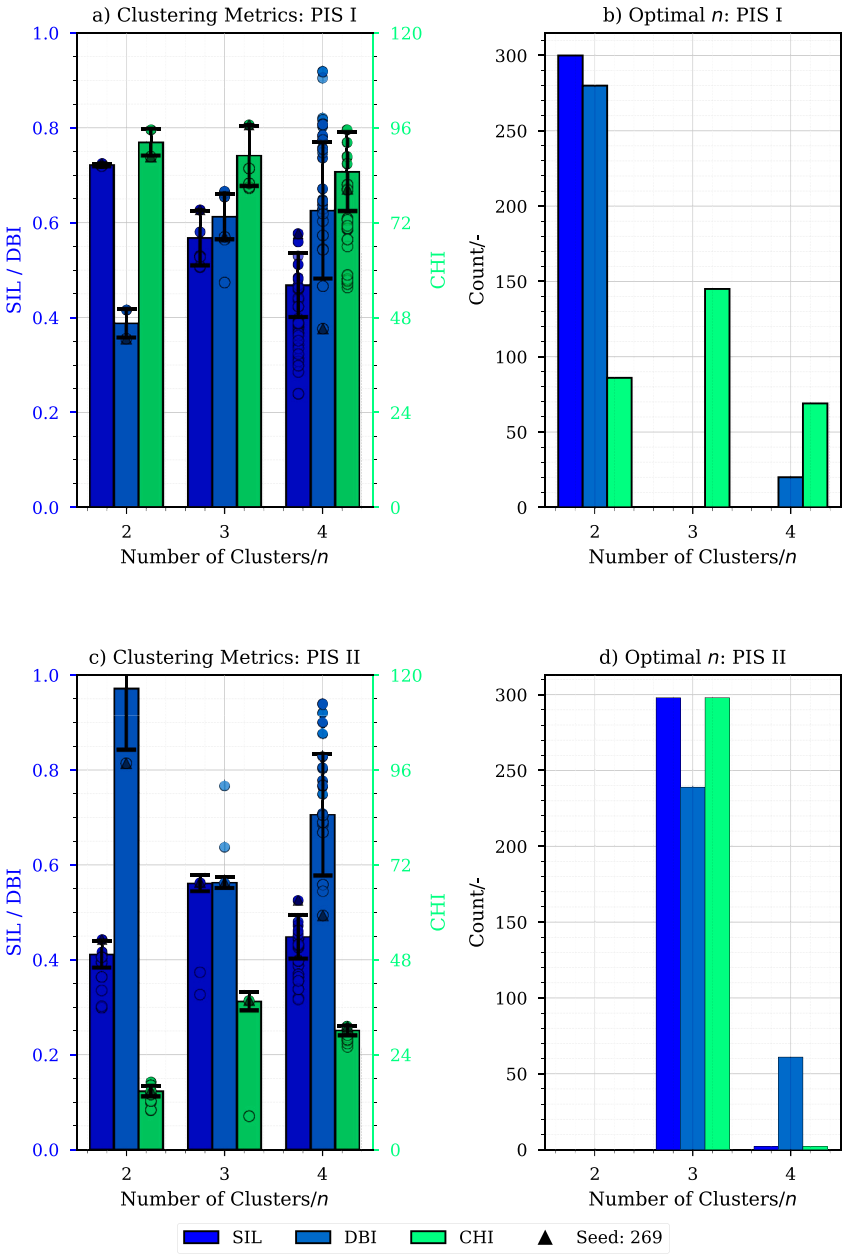

Fig. 5. Clustering analysis results for PIS I and PIS II. (a, c) Mean values of the SIL, DBI, CHI scores over 300 clustering runs with different random seeds, shown as bar plots for 2, 3, and 4 clusters. Individual points contributing to the mean values are overlaid as scatter plots. Black lines indicate the standard deviation of the metrics, and the black triangle marks the metric values obtained with a random seed of 269. (b, d) Optimal number of clusters selected by SIL, DBI, and CHI over 300 clustering runs with different random seeds. (For interpretation of the references to color in this figure legend, the reader is referred to the web version of this article.)

reducing or CHI monotonically increasing. Therefore, only the results of the analysis performed on n values up to 4 is reported.

For PIS I, as seen in Fig. 5a the maximum average value of SIL is around 0.7 and the lowest average value of DBI is around 0.4 for $n = 2$. The average value of CHI is mostly around 90 for both $n = 2$ and $n = 3$. Therefore, averaging across 300 random seeds, 2 out of 3 metrics would consistently select $n = 2$ as optimal number of clusters. This is confirmed by Fig. 5b, which shows that SIL always selects $n = 2$, DBI selects it for 280 out of the 300 random seeds, while CHI's selections are more unstable and it generally selects $n = 3$. Finally, for a $n = 2$, the three metrics only take 2 possible values over the 300 random seeds as seen by the narrow distribution of the points in the figure. This indicates that there are two ways to cluster PIS I into two clusters. In this study, a random seed that resulted in SIL value of 0.724, DBI value of 0.355 and CHI value of 88.596 for $n = 2$ is described along with the clusters identified for $n = 3$.

For PIS II, as seen in Fig. 5c the maximum average value of SIL and DBI is around 0.56 and the highest average value of CHI is around 37 for $n = 3$. Therefore, averaging across 300 random seeds, all of the metrics would consistently select $n = 3$ as optimal number of clusters. This is confirmed by Fig. 5d, which shows SIL and CHI always select a n value of 3 for 298 seeds and DBI selects it for 240 seeds. Finally, for $n = 3$, the three metrics often fall on the same value except for a few outliers. This indicates that there is a single way to cluster PIS II into three clusters. In this study, a random seed that resulted in SIL value of 0.562, DBI value of 0.561 and CHI value of 37.656 for $n = 3$ is described along with the clusters identified for $n = 4$.

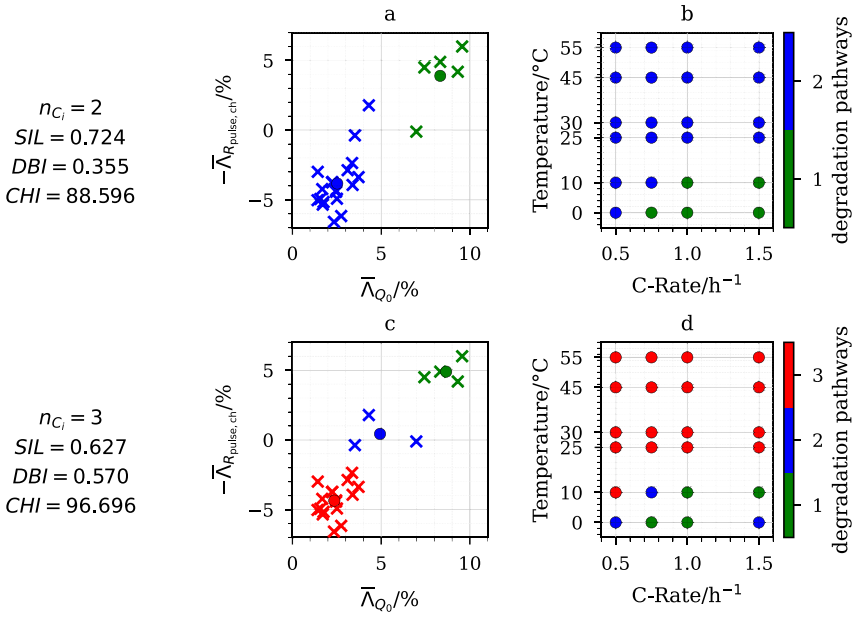

Fig. 6. PIS I and SFS after performing clustering analysis for two different predefined cluster values. The values of the relative change in the degradation metrics are represented by 'x' in the PIS, with the points belonging to one cluster having the same color. The center of the clusters are marked by a circle of the same color. The tested points in the SFS are marked by a circle and the color of the circle represents the degradation pathway that the particular stress factor causes. (a) PIS I (Λ_{Q_0} vs $\Lambda_{R_{pulse,ch}}$) for 2 predefined clusters, (b) SFS of space I for 2 predefined clusters, (c) PIS I (Λ_{Q_0} vs. $\Lambda_{R_{pulse,ch}}$) for 3 predefined clusters, (d) SFS of space I for 3 predefined clusters.

4.3.2. Path-indicator space I: $\bar{\Lambda}_{Q_0}$ and $\bar{\Lambda}_{R_{pulse,ch}}$

Clusters are generated using PIS based on $\bar{\Lambda}_{Q_0}$ and $\bar{\Lambda}_{R_{pulse,ch}}$. In Fig. 6a, the results for clustering is shown for a cluster size of two, which resulted in a silhouette score of 0.72. The individual points are marked with an 'x', with the color of the each point representing the cluster, i.e. a degradation pathway. The corresponding cluster centers are marked by filled circles. The first identified degradation pathway, marked with green, can be found in a region where $\bar{\Lambda}_{Q_0}$ is large and $\bar{\Lambda}_{R_{pulse,ch}}$ is positive. In this pathway, the $\bar{\Lambda}_{Q_0}$ is above 6% and the $\bar{\Lambda}_{R_{pulse,ch}}$ is above 0%. The second pathway, marked in blue, is found at a region where $\bar{\Lambda}_{Q_0}$ is smaller than 4% and $\bar{\Lambda}_{R_{pulse,ch}}$ is negative.

Another clustering of PIS I is shown in Fig. 6c. However, here three clusters are used, which corresponds to a silhouette score of 0.63, being smaller then a clustering with only two clusters. The first degradation pathway, marked with green, is found at a region where with large $\bar{\Lambda}_{Q_0}$ and positive $\bar{\Lambda}_{R_{pulse,ch}}$. In this region, the $\bar{\Lambda}_{Q_0}$ is above 6% and the $\bar{\Lambda}_{R_{pulse,ch}}$ is above 4%. The second pathway, marked in blue, is found in the middle region and was previously split into the two clusters. In this region, the $\bar{\Lambda}_{Q_0}$ is between 3%–7% and the $\bar{\Lambda}_{R_{pulse,ch}}$ is between 0%–2%. The third pathway, marked in red, is found at a region where $\bar{\Lambda}_{Q_0}$ is lower than 4% and $\bar{\Lambda}_{R_{pulse,ch}}$ is lower than −2%.

To confirm whether the identified pathways can be triggered by particular regions in the SFS, they are mapped onto their corresponding locations in the SFS.

Fig. 6b and d illustrates the SFS for two and three clusters, respectively. The individual points represent the conditions tested in this study and the color of the point represents the identified pathway.

In Fig. 6b, the identified degradation pathways for two clusters are shown. The first degradation pathway, marked with green, can be found both at 0 °C and 10 °C. At 0 °C, it occurs at a C-rate greater than 0.75 C. At 10 °C, it occurs at a C-rate greater than 1 C. Considering the temperature and C-rates at which this pathway appears, the underlying cause for it is probably low temperature aging mechanisms such as lithium plating that leads to processes that cause rise in the pulse resistance [4,18]. The second pathway marked with blue can be found at all temperatures. Between 25 °C and 55 °C, it appears at all C-rates. At 0 °C, it appears at 0.5 C and at 10 °C it appears at 0.5 C and 0.75 C. Since, the region above 25 °C is entirely identified as pathway 2, indicates that this pathway is likely a high temperature degradation pathway including mechanisms such as SEI growth [87]. However, this pathway also seems to appear at some C-rates (0.5 C, 0.75 C) for temperature values less than 10 °C. Possibly, with only two clusters, the aging pathway at low temperature and low C-rates cannot be discriminated from aging pathways at other temperatures.

In Fig. 6d, the identified degradation pathways for three clusters are shown in the SFS. The first pathway, marked with green, can be found both at 0 °C and 10 °C. At 0 °C, it occurs at a C-rates of 0.75 C and 1 C. At 10 °C, it occurs at a C-rate of greater than 1 C. The second pathway, marked with blue, appears at 0 °C for C-rates of 0.5 C and 1.5 C and at 10 °C for a C-rate of 0.75 C. It is evident from the Figure that the region bounding these points is not continuous as it is interrupted by pathway 1 (green) in the SFS. In the PIS both regions appear similar, but in the SFS they are not close to each other. This observation indicates that this cluster is most likely not a separate pathway but more likely similar to the green pathway, just with less intense degradation. It is noted that confirming this hypothesis is out of the scope of this work. The third pathway, marked with red, appears at all temperatures above 25 °C and at 10 °C and a C-rate of 0.5 C. The fact that the region above 25 °C is entirely assigned to it, indicates that this pathway is likely a high temperature degradation pathway.

To conclude, clustering with PIS I enables to differentiate high and low temperature aging pathways and enables to identify two distinct clusters. With three clusters the pathways are no longer connected in the SFS, indicating that the third cluster is not really a different degradation pathway, but rather belongs to one of the other two clusters. This conclusion is also supported by a lower silhouette score.

This results are in agreement with previous works that were able to use a similar 2D space to discriminate high- and low temperature aging mechanisms [36,37]. It is emphasized that the method used in this study is able to automatically discriminate these regions from only a short-term aging study and does not use the stress condition, e.g. temperature, as prerequisite for the clustering, even though a similar cluster would be achieved by just separating the SFS into low and high temperature regions.

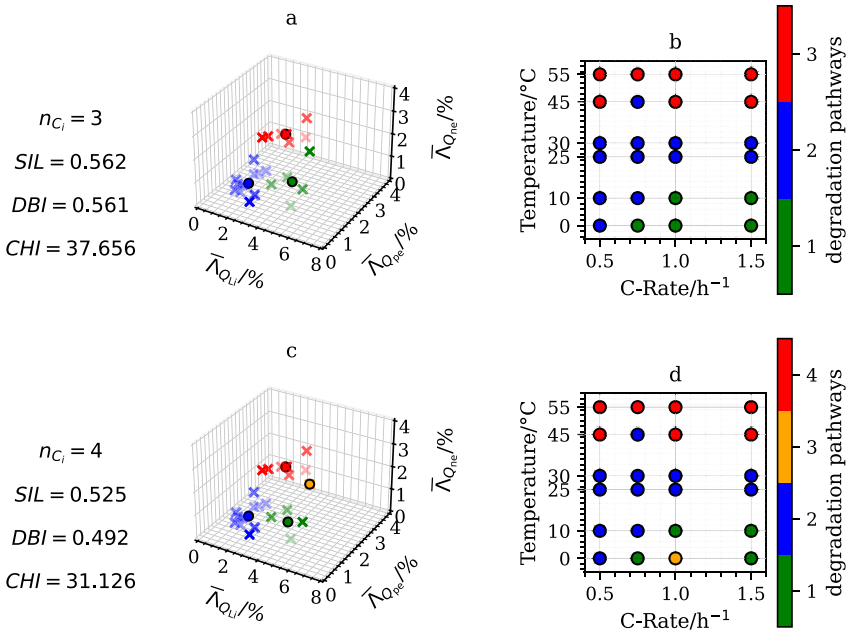

Fig. 7. PIS II and SFS after performing clustering analysis for two different predefined cluster values. The values of the relative change in the degradation metrics are represented by 'x' in the PIS, with the points belonging to one cluster having the same color. The center of the clusters are marked by a circle of the same color. The tested points in the SFS are marked by a circle and the color of the circle represents the degradation pathway that the particular stress factor causes. (a) PIS II ($\Lambda_{Q_{Li}}$ vs. $\Lambda_{Q_{pe}}$ vs. $\Lambda_{Q_{ne}}$) for 3 predefined clusters, (b) SFS of space II for 3 predefined clusters, (c) PIS II ($\Lambda_{Q_{Li}}$ vs. $\Lambda_{Q_{pe}}$ vs. $\Lambda_{Q_{ne}}$) for 4 predefined clusters, (d) SFS of space II for 4 predefined clusters,.

4.3.3. Path-indicator space II: $\bar{\Lambda}_{Q_{Li}}$, $\bar{\Lambda}_{Q_{pe}}$ and $\bar{\Lambda}_{Q_{ne}}$

In this section clusters are generated using a PIS based on degradation modes, i.e. $\bar{\Lambda}_{Q_{Li}}$, $\bar{\Lambda}_{Q_{pe}}$, and $\bar{\Lambda}_{Q_{ne}}$. Results for a cluster size of three are shown in Fig. 7a. This corresponds to a silhouette score of 0.56. The individual points are marked with an 'x', with the color representing the identified degradation pathway. The cluster centers are marked by filled circles. The first degradation pathway, marked with green, is found at a region where $\bar{\Lambda}_{Q_{Li}}$ is above 4%, $\bar{\Lambda}_{Q_{pe}}$ is below 1%, and $\bar{\Lambda}_{Q_{ne}}$ is between 0%–3%. The second pathway, marked in blue, is found at a region where $\bar{\Lambda}_{Q_{Li}}$ is smaller than 4% $\bar{\Lambda}_{Q_{pe}}$ is between 0%–2%, and $\bar{\Lambda}_{Q_{ne}}$ is between 0%–1%. The third pathway, marked in red, is found at a region where $\bar{\Lambda}_{Q_{Li}}$ is between than 2%–4% the $\bar{\Lambda}_{Q_{pe}}$ is between 2%–4%, and the $\bar{\Lambda}_{Q_{ne}}$ is between 1%–3%. These three clusters are visually distinct from each other, but they are not as compact as the clusters identified in the PIS I. Nevertheless, a silhouette score value larger than 0.5 is still considered a good quality cluster. Here, the PIS is defined by degradation metrics that represent the aging state of both electrodes, which enables a more detailed clustering. For example, pathway 2 is caused by aging mechanisms that cause both $\bar{\Lambda}_{Q_{Li}}$, $\bar{\Lambda}_{Q_{pe}}$ but not a lot of $\bar{\Lambda}_{Q_{ne}}$. In, contrast pathway 1 shows lower $\bar{\Lambda}_{Q_{pe}}$ but higher $\bar{\Lambda}_{Q_{Li}}$. Pathway 3 is caused by aging mechanisms that cause all of the degradation modes.

In Fig. 7c, results for a cluster size of four are shown, which corresponds to a silhouette score of 0.52, being slightly lower than for three clusters. The clustering appears similar to the clustering with three cluster as discussed before. However, one point of previous pathway 1 is now assigned to an additional pathway (here pathway 3), marked in orange. Degradation pathways are well separated from each other but they are not as compact as the clusters identified in PIS I, as can be seen by the lower silhouette score. Nevertheless, a silhouette score value of above 0.5 is still considered a good quality cluster.

To further investigate the identified pathways, they are again mapped to the SFS. Results are shown Fig. 7b and d for three and four clusters, respectively.

In Fig. 7b, the identified degradation pathways for three clusters is shown. The first degradation pathway can be found both at 0 °C and 10 °C. At 0 °C, it occurs at a C-rate of greater than 0.75 C. At 10 °C, it occurs at a C-rate of greater than 1 C. This cluster is equivalent to the first pathway identified with PIS I with two clusters, which supports the clear distinction of this region from the other regions. In terms of degradation mechanisms, lithium plating, is a plausible underlying mechanism as it leads to both high loss of lithium inventory and negative electrode active material [18,80]. The second pathway, marked with blue, can be found at temperatures varying from 0 °C to 30 °C. At 25 °C and 30 °C, it appears at all C-rates. At 0 °C, it appears at 0.5 C and at 10 °C, it appears at 0.5 C and 0.75 C. There is a single point at 0.75 C and 45 °C. This pathway is caused by a cluster with low values of the degradation modes. As such, this region forms a transition zone between the low temperature and high temperature aging. The third pathway, marked with red, is found at temperatures greater than 45 °C, except for 0.75 C and 45 °C. Considering the temperatures at which this pathway appears, this is most likely caused by high temperature aging mechanisms such as SEI growth and loss of active materials at both of the electrodes [87].

In Fig. 7d, the degradation pathways for a cluster size of 4 is shown in the SFS. The degradation pathways 1,2,4, marked with green, blue, and red, respectively, are found at the same positions as previously. Pathway 3, marked with orange, is a single point located at 0 °C and 1 C. Considering the temperatures at which this pathway appears, the underlying mechanisms for it is likely the same or similar to the degradation pathway 3 (green), might only be different in intensity. However, it is also possible that additional mechanisms become active here, which would correspond to another aging pathway that starts at 0 °C and 1 C. Confirmation, would require more tests at temperatures less than 0 °C, which is out of the scope of this work.

In summary, it can be seen that clustering PIS with degradation modes can be used to identify at least three clusters. All cluster points are also connected in the SFS, which supports the conclusion that different degradation pathways have indeed been identified. A fourth degradation pathway may be present at low temperatures, i.e. pathway 3 with four clusters.

4.3.4. Summary of degradation pathway identification

In summary, by depicting the degradation metrics in a 2D and a 3D PISs (PIS I and PIS II) and conducting a clustering analysis on these points, different degradation regimes can be found in the data. The points in these clusters can then be mapped onto a SFS, which leads to regions in the SFS that could be utilized to trigger unique degradation pathways.

Clustering analysis is done on PIS I and II and lead to high values of the silhouette score. In both cases, a region at low temperatures ($\leq$10 °C) and high C-rates (>0.75 C) is identified as one degradation pathway. Further segmentation of the points in PIS I, identifies a noncontiguous region in the SFS that consists of low temperatures and low C-rate and one point at low temperature and high C-rate. This is an indicator that this region does not cause a unique degradation pathway. However, PIS II, allows to identify another region so that it can be further separated into a pathway that includes low temperatures and low C-rates and moderate temperatures, and another pathway at high temperatures.

As described in Section 3.5, two cells were used per aging condition in this study. In Section 4.1, the trends of the DMs with temperature and C-rates were discussed. While these trends are usually caused by a specific degradaton pathway that is triggered by the applied aging condition, they also include the impact of differences in the internal states the cells at BOL upon the triggered degradation pathway. The small sample size means that the confidence intervals of the DMs used to build the PIS can be large. Nevertheless, based on the work described in this section, the observed trends in the DMs are sufficient to separate SFS into regions that trigger different DPs. Future work that performs a study using a larger number of samples per aging condition might result in a PIS where the points are more clearly separated due to narrower confidence intervals and as a result becoming easier to cluster. Additionally, a larger sample size could also aid in improving statistical significance to the trends in the DMs.

It should be noted that, the tested cell type consisted of graphite negative electrode and an NMC based positive electrode. Degradation pathways in general are expected to be impacted by the materials and the operating conditions. For example, Si-blended electrodes show larger loss of Silicon when cycled at a lower SOC range [13]. Batteries consisting of NCA electrodes [20] and LFP electrodes have been shown to exhibit path-dependency [82]. It is possible that under the same operating conditions, another material combination might show different aging pathways. Nevertheless, the methodology used to identify aging pathways in this work should be generalizable to any existing or novel chemistries as long as an appropriate PIS and SFS can be identified for it. Applying this method to other chemistries can be addressed in future work.

This work builds on the use of multidimensional features such as PIS I [36,37] and PIS II [88] to distinguish degradation pathways, introducing three key improvements. First, the clustering-based framework automates pathway identification and employs validity metrics (SIL, DBI, CHI) to evaluate their quality, reducing reliance on manual interpretation in earlier approaches [36]. Second, the method generalizes the definition of PISs to any *n*-dimensional representation. This enables the inclusion of any kind of degradation information (e.g., EIS, NFRA) for separating degradation pathways, which means that the method is not limited by the features used in PIS I and II. Third, by incorporating a common dimension such as time or charge throughput, the framework can capture transitions in degradation pathways, reflecting the fact that a given stress condition may induce different pathways at beginning and end of life.

Therefore, the clustering based framework allows for a non-destructive, systematic mapping of the relationship between stress factors and degradation pathways. Additionally, the clusters identified by this method can be stored as a look-up table in a battery management system and sensor information measured from cells can be used to identify the aging pathway of the cell during operation and react to transitions of a cell's degradation to pathways that lead to faster degradation.

The quality of the clusters identified by the framework might depend on the PIS. As the number of clusters is a predetermined value, there is a potential for over clustering of the PIS into meaningless clusters, which can be carefully negated by considering the different clustering metrics and the contiguity of the identified clusters in the SFS. Finally, the clusters may also arise from distinct aging mechanisms or from different impact of similar mechanisms on the cell. Distinguishing between these cases requires expert knowledge and post-mortem analysis. In Section 4.4, microscope analysis and DRT analysis are used to show that the degradation pathways identified by the cluster analysis are actually unique and likely result from different degradation mechanisms. Here, we investigate PIS II with three clusters.

4.4. Validation

In this section, the degradation pathways that were identified by performing clustering analysis on PIS II using three predefined clusters are analyzed further by optical microscopy and DRT analysis. For optical microscopy, the negative electrode of one cell belonging to each cluster is chosen that is farthest away from the centers of the other clusters. The negative electrode is investigated, because SEI growth and Li plating are the likely dominant degradation mechanisms at the chosen operating conditions [4,18]. Both occur at the negative electrode, while Li plating is usually well visible during optical inspection [18,26]. The DRTs of these cells are also analyzed and a qualitative interpretation is performed to see the differences.

4.4.1. Optical microscopy

Fig. 8a (uncycled cell),b (degradation pathway 1), c (degradation pathway 2), and d (degradation pathway 3) show microscope images of the negative electrode of a cell that has not undergone any cyclic aging and one cell tested at one representative test condition from a degradation pathway. The condition is selected from the three degradation pathways identified in Fig. 7b. This selection is performed by firstly calculating the distance of each points in the PIS II to the three cluster centers. Subsequently, one point in each cluster is selected that is farthest away from the other cluster centers. This point is mapped to its corresponding location in SFS, and a cell aged under this condition is opened under the glovebox atmosphere. These cells have been tested at 1 C and 0 °C for degradation pathway 1, 1 C and 30 °C for degradation pathway 2. 0.5 C and 45 °C for degradation pathway 3. The images bounded by solid rectangles provide an overview of the electrode, and it was generated by making a compilation out of multiple images. It is noted that the compiled image is included to illustrate general trend of the uncycled cell and different degradation pathways. Selected parts of the compiled images are shown to the right and bounded by dashed rectangles and they correspond to the overview image as indicated. The color of the dashed rectangles refers to the degradation pathway as provided in Fig. 7, with a green rectangle representing pathway 1, blue rectangle representing pathway 2, and red rectangle representing pathway 3. The black rectangle corresponds to the uncycled cell.

The negative electrode of the uncycled cell is shown in Fig. 8a. In general, the electrode looks bright and relatively unblemished. There are some bright lines visible in the electrode along with some few darker areas. These darker regions are however only found in three of the 40 images that were captured of the electrode surface, indicating that they do not occur regularly. This is shown in the selected images that are bounded by black dashed rectangle. The image from side 1 shows that the darker part of the electrode look mostly similar to the surrounding area in terms of morphology. The image from side 2 has a similar region in the center of the image that is darker as compared to rest of the electrode. Both the chosen images show some small white spots on the surface of the electrode.

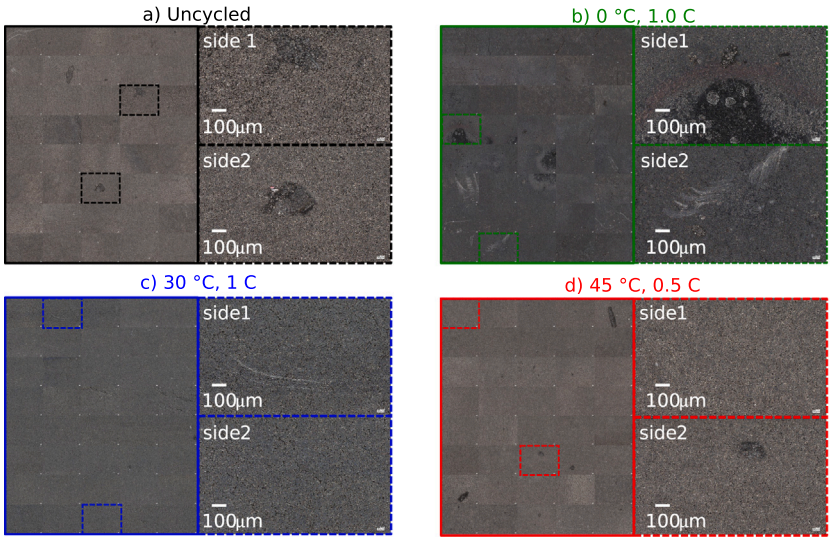

Fig. 8. Microscope images of the two sides of the negative electrode for selected cells that belong to the three identified degradation pathways using PIS II and an uncycled cell. (a) Overview image of a cell belonging the an uncycled cell, bounded by a solid black rectangle and two selected images from two sides of the electrode of this cell bounded by dashed black rectangle.(b) Overview image of a cell belonging the degradation pathway 1, bounded by a solid green rectangle and two selected images from two sides of the electrode of this cell bounded by dashed green rectangle. (c) Overview image of a cell belonging the degradation pathway 2, bounded by a solid blue rectangle and two selected images from two sides of the electrode of this cell bounded by dashed blue rectangle. (d) Overview image of a cell belonging the degradation pathway 3, bounded by a solid red rectangle and two selected images from two sides of the electrode of this cell bounded by dashed red rectangle.

The negative electrode of cell from pathway 1 is shown in Fig. 8b. The general appearance is rather dark and heterogeneous. There are signs of surface deposits in the form of thick silver lines and smaller circular deposits on top of the electrodes. Additionally, parts of the electrodes seem much darker compared to the rest of the electrodes. This is clearly visible in the selected images that are bounded by the green dashed rectangle. The image from side 1 shows the dark parts of the electrode in the bottom half of the image. There are small circular spots that seem to be on top of the electrode in the center of the image. The image from side 2, shows a thick silvery region that starts at the top-right corner of the image and ends in a large deposit that looks very different from the rest of the electrode. In comparison to the uncycled cell, this surface looks darker and more degraded.

The negative electrode of a cell from pathway 2 is shown in Fig. 8c. In general, it appears brighter and less heterogeneous than images for pathway 1. There are signs of surface deposits in form of white lines, but no circular deposits are visible. The electrode shows small dark gray spots. This is clearer in the selected images that are bounded by the blue dashed rectangle. The image from side 1 shows white lines at the center of the image, but the rest of the image shows an electrode that has a rather uniform coloration. The image from side 2 does not show any sign of surface deposits. In comparison to the uncycled cell, this surface looks darker and also it has a minimal dark spots on the electrode surface.

The electrode belonging to pathway 3 is shown in Fig. 8d. There are no signs of surface deposits, except for more dark spots in parts of the electrodes. There seems to be sort of a gradient in the color of the electrodes. Some features are visible upon closer inspection of the electrodes. The image from side 1 shows small white circular regions, which are distributed throughout the image. The image from side 2 shows circular dark gray spots at the top-right corner of the image and there are white spots that are visible in different parts of the image. It can be seen that these white spots are also of rather uniform size. In comparison to the uncycled cell, this surface looks most similar in terms of the color. However, it has more darker spots on the electrode surface.

The qualitative trends visible in the images are complemented by analyzing the distribution of their pixel intensities. In order to get a more quantitative insight, 40 images from different positions in the electrodes of the uncycled cell and the cell belonging to pathway 1–3 is converted to a gray scale and the overall count of each pixels that correspond to a particular intensity is used to build the normalized histogram shown in Fig. 9. The black bar in the histogram represents the uncycled cell. The green corresponds to the cell that aged with pathway 1, the blue bar corresponds to the cell that aged with pathway 2, and the red bar corresponds to the cell that aged with pathway 3.

In general, the electrode from the uncycled cell shows a broad distribution that has around 20% of its pixels in the 51–75 range, 32% of its pixels in the 76–101 intensity range and around 22% of its pixels in the 102–127 intensity range, with lower contributions at higher intensities. The broad nature of the distribution is an indicator of a relatively unaged electrode.

The electrode of the pathway 1 cell shows a narrower distribution, with a tall peak in the 51–75 range that contains 46% of its pixels. In this range, the cell has around 24% more pixels than the uncycled cell, 20% more pixels than the pathway 2 cell and 17% more pixels than the pathway 3 cell. In the 76–101 range, the pathway 1 cell shows 5% less pixels than the uncycled cell and around 8% less pixels than the pathway 2 cell and 7% less pixels than the pathway 3 cells. The proportion of pixels for this pathway drops significantly at an intensity greater 102. This indicates that the electrode from pathway 1 is clearly dominated by darker regions as compared to the other electrodes.

The electrode from the pathway 2 cell shows a similar distribution as the uncycled cell and shows a peak in the 76–101 intensity range where 35% of its pixels exist. The electrode also has around 20% of its pixels in the 102–127 intensity range after which the pixel contributions drop. This electrode is moderately darker than the uncycled cell as it has around 4% more pixels in the 51–75 and 76–101 intensity ranges. It is also significantly brighter than the pathway 1 cell, considering the difference in the proportion of pixels in the 51–75 range. Therefore, this electrode seems to show a combination of features from the uncycled and the pathway 1 cell.

Finally, the electrode from the pathway 3 cell shows a similar distribution as the uncycled and pathway 2 cell and has a peak contribution of around 33% of the total pixels in the 76–101 range. It matches the pixel contributions of the uncycled electrode upto the 51–75 intensity

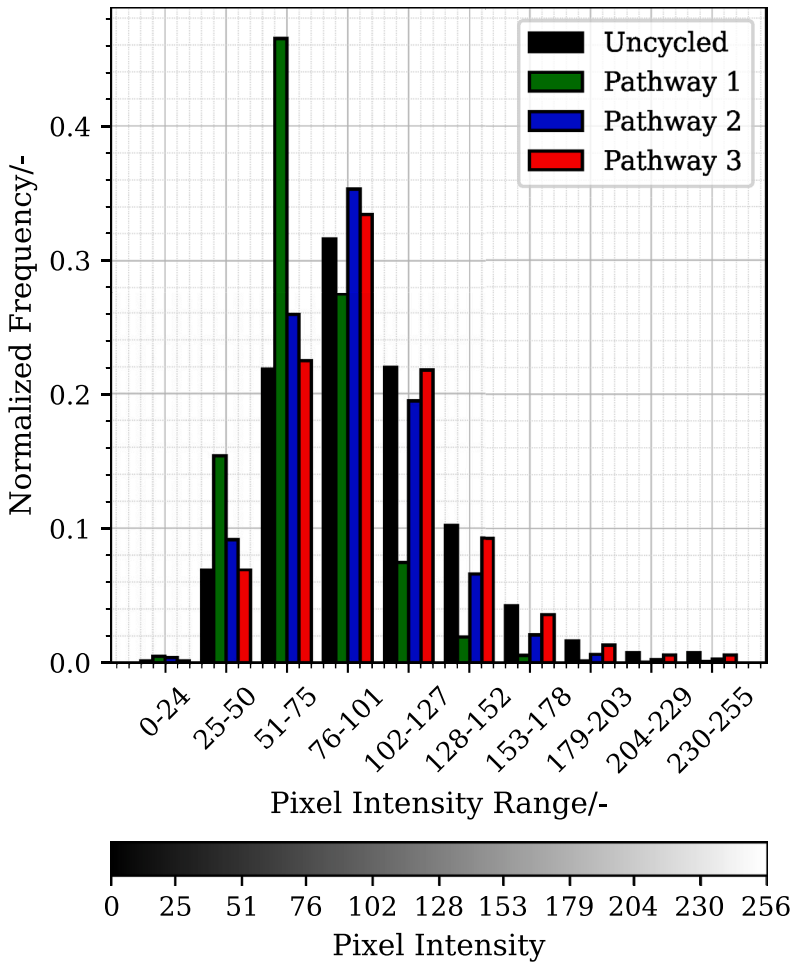

Fig. 9. Distribution of the pixel intensities of the uncycled cells (black) shown along with the distributions of Degradation Pathway 1 (green), Degradation Pathway 2 (blue), Degradation Pathway 3 (red).

range. It has around 2% more pixels in the 76–101 range as compared to the uncycled cell, which matches the general trend of the aged electrodes have higher proportions of darker pixels in comparison to the uncycled electrode. In contrast to the other aging pathways, it has around 10% of its pixels in the 128–152 range. This indicates that this electrode is similar to the uncycled cell except for some darker spots. It also has some brighter spots as compared to the electrodes from the other two pathways.

The uncycled electrode looked mostly pristine and unblemished as it had not experienced any cyclic aging. Based on the images only, it is difficult to identify the reasons for the darker areas. They could be defects on the surface of the electrode or some kind of decomposition products formed on the surface during storage. The large circular silver deposits found on top of the electrode of the cell belonging to pathway 1 are most likely plated lithium in the form of dendrites. These deposits are also not uniformly bright and has several darker points, which likely contribute to a significant proportion of pixels belonging to the darker intensity range as compared to the cells from other pathways. Nevertheless, it can be clearly distinguished from the underlying graphite particles. Additionally, such silver-colored dendrites have been observed from optical microscopy images in several studies [89–91]. The thick silvery lines on the electrode might also be plated lithium that has a different morphology [18,92]. It is difficult to identify the underlying cause for the darker spots in the electrode by only optical inspection. Nevertheless, these observation cannot be made for any of the other degradation pathways.

The silvery-white lines are also visible for the cell belonging to pathway 2 but not to a large extent. At the same time, there are few places that have dark gray/brown spots, which likely contribute to the moderate darkening of this electrode in comparison to the uncycled cell. This was attributed to electrolyte decomposition by Rangarajan et al. [72] and they say this indicates SEI growth. But for this cell, only few of these spots are visible.

The small white spots that are visible throughout the electrode belonging to pathway 3 is likely some kind of electrolyte product that was still left on the surface of the electrode. The existence of these white spots on the electrode is more for the pathway 3 cell than the pathway 2 or 1 cell as confirmed by the higher proportion of pixels in the brighter intensity range. Finally, the overview images show a difference in the color between the electrodes aged using different pathways, even though it cannot be interpreted reliably without further postmortem analysis.

To summarize, the electrodes belonging to the different pathways look visually different and therefore confirming that these cells have undergone different degradation pathways. The electrode at pathway 1 shows clear signs of surface deposits that could be lithium plating and this electrode surface is significantly darker as compared to the uncycled electrode and the electrodes aged at pathway 2 and 3. The electrode at pathway 2 has these white lines that were also found on the electrodes in pathway 1. Additionally, few spots were found in the electrode that had some kind of gray/brown decomposition products. The electrode showed signs of darkening in comparison to the uncycled electrode in the 51–75 pixel intensity range but had still more proportion of pixels in the 76–101 range as compared to pathway 1. This could be an indicator that the cells in this pathway undergo

Table 1
Changes in polarization and time constant for three degradation pathways, with BOL values used as the reference. Increasing time constants correspond to slower processes and polarization is defined as the sum of polarization for one Gaussian peak.

	DP 1 (0 °C, 1 C)		DP 2 (30 °C, 1 C)		DP 3 (45 °C, 0.5 C)	
	Pol.	τ	Pol.	τ	Pol.	τ
Cell 1	27%	23%	8%	66%	−40%	102%
Cell 2	48%	23%	−31%	113%	−46%	92%
Mean	37%	23%	−12%	90%	−43%	97%
Trend	↑ Increase	↗ Mod. slower	↘ Mod. decrease	↑ Slower	↓ Decrease	↑ Slower

a mixture of aging pathway 1 and 3. Finally, the electrode from the aging pathway 3 has uniform white deposits all over the electrode. The pixel distribution of this electrode looked mostly similar to the uncycled electrode but it had higher proportion of pixels in the 102–255 intensity range as compared to the electrodes from the other pathways. This indicates that the three aging pathways identified by our method lead to different kind of degradation that is visible at the electrode level, but confirming the exact mechanism would require a detailed postmortem analysis that is beyond the scope of this work.

4.4.2. Distribution of relaxation times

Fig. 10 shows the distribution function and the peak fit for two cells selected from each degradation pathway. These cells have been tested at 1 C and 0 °C for degradation pathway 1, 1 C and 30 °C for degradation pathway 2. 0.5 C and 45 °C for degradation pathway 3. Within each plot, the evolution of the characteristic peaks between BOL and the EOL are compared. To improve visibility of the mid-frequency region, the low-frequency part of the distribution function covering the diffusive branch is excluded from the presentation.

Within this range of time constants, the DRT analysis shows multiple peaks, one of which is resistive-inductive and the others of which are resistive-capacitive. The resistive-capacitive peaks are arranged in increasing order of polarization, with a dominant peak occurring at approximately 0.3 ms.

According to the literature [50], this main peak can be primarily attributed to the charge transfer process occurring at the anode and/or cathode. The neighboring peaks with larger time constants, which are not fully visible in the figure, are assigned to the diffusive branch [50]. Identifying and assigning single peaks to electrochemical processes occurring inside a battery is challenging. It requires a multidimensional parameter variation (e.g. temperature, SOC) as well as half-cell measurements to distinguish between processes at an electrode level [50], as well as expertise in interpretation, since multiple processes can be interconnected and thus influence multiple peaks simultaneously due to possible inference and linkage [93]. This is beyond the scope of this work, making it impossible to reliably identify and separate the processes of each electrode. That being said, the focus will be on the dominant peak, which is shaded in blue, and how it is affected by the different degradation pathways.

In Table 1 the relative change of polarization and time constant is shown for the three degradation pathways. The BOL counts as the base value and the polarization of the investigated peak is defined as the summed polarization of the Gaussian peak according to Eq. (12). Despite expected cell-to-cell variations between the samples of each group, trend indications can be observed:

Degradation pathway 1 Within this aging path the polarization of the two samples increases by an average of 37% while the time constant increases by 23%. Compared to the other DPs, this is the only one showing an increase in polarization. Further, the change in time constant is smaller.

Degradation pathway 2 This group shows a similar slowdown of the process (90%) compared to DP 3. The change in polarization falls between 8% and −31%, meaning that one cell shows an increase in resistance, while the second cell shows a decrease. On average, this group tends towards a slight decrease.

Degradation pathway 3 The time constants within this group are comparable to DP 2 with an average increase of 97%. However, this time the polarization is decreasing by −43% between BOL and EOL measurement.

From the analysis, it is evident that the distribution functions of the cells at degradation pathway 1 show a different behavior than the cells at 2 and 3. The polarization of the characteristic peak increases significantly and the process becomes moderately slower. Based on the fact that the cell at pathway 1 showed signs of surface deposits that is likely caused by lithium plating, it is likely that this has led to an increase in the overall polarization of the cell leading to an increase in the resistance of the charge transfer reaction and the transport through the passivating layers.

There are also differences between the DRT of pathway 2 and 3 but it is harder to identify the possible reasons for it. The polarization of the characteristic peak decreases more for pathway 3 in comparison to pathway 2. It was earlier hypothesized that the reduction of resistance observed in this work arises from the possibility of microcracking of particles [78]. It is possible that these cracks happen more for pathway 3 than for pathway 2, leading to a sharper drop of the polarization resistance. Additionally, the moderate reduction to the polarization of the characteristic peak for pathway 2 could indicate that this pathway is between 1 and 3.

The time constants of the characteristic peak appears to slowdown for both pathway 2 and 3. This effect is more pronounced in pathway 3 compared to pathway 2, suggesting a greater slowdown of the kinetics of the processes associated with the characteristic peak. At the same time, the intensity of the polarization peak decreases more in pathway 3 than in pathway 2, indicating a larger reduction in the resistance of the corresponding processes. While this highlights an inherent difference between aging pathways 2 and 3, the underlying causes remain unclear. A more detailed investigation is required to fully understand these observations and is proposed as future work.

4.4.3. Summary

To summarize, cells were chosen from a representative test condition that is selected from the three identified degradation pathways. DRT of the cells tested at one representative test condition that is selected from the three degradation pathways identified in Fig. 7b was analyzed. It is clear, that the cell that undergoes degradation pathway 1 behaves very different compared to 2 and 3, considering the signs of lithium deposition that was visible in the microscope images and the overall increase in the polarization of the cell in the DRT. This correlates well with the fact that this cell belonged to the pathway that showed high LLI (~6%) and LAM_{NE} (~3%) with minimal LAM_{PE} (~<1%), which indicates that it underwent significant degradation.

The microscope image of the anode of the cell that underwent degradation pathway 2 showed some signs of surface depositions that could be deposited lithium or other kinds of decomposition products. This cell also showed a moderate reduction in polarization and a slow down of the characteristic peak in the DRT. This could mean that the cell only shows minimal signs of degradation, which is reflected in the fact that this cell showed minimal LLI (~<1%), LAM_{NE} (~<1%) and LAM_{PE} (~<1%). In comparison, the anode of the cell that underwent degradation pathway 3 had uniformly distributed white spots of the same size and more signs of other kinds of decomposition products. The DRT of the cells from these degradation pathways also show larger amount of changes to the intensity and the time constants of characteristic polarization peak that was considered for the analysis in comparison to degradation pathway 2. This means that the cell showed signs of more degradation than the cell from pathway 3 but much less than the cell from pathway 1, which is evident in the calculated DM's for the cell, which showed moderate LLI (~2%), LAM_{NE} (~2%), and

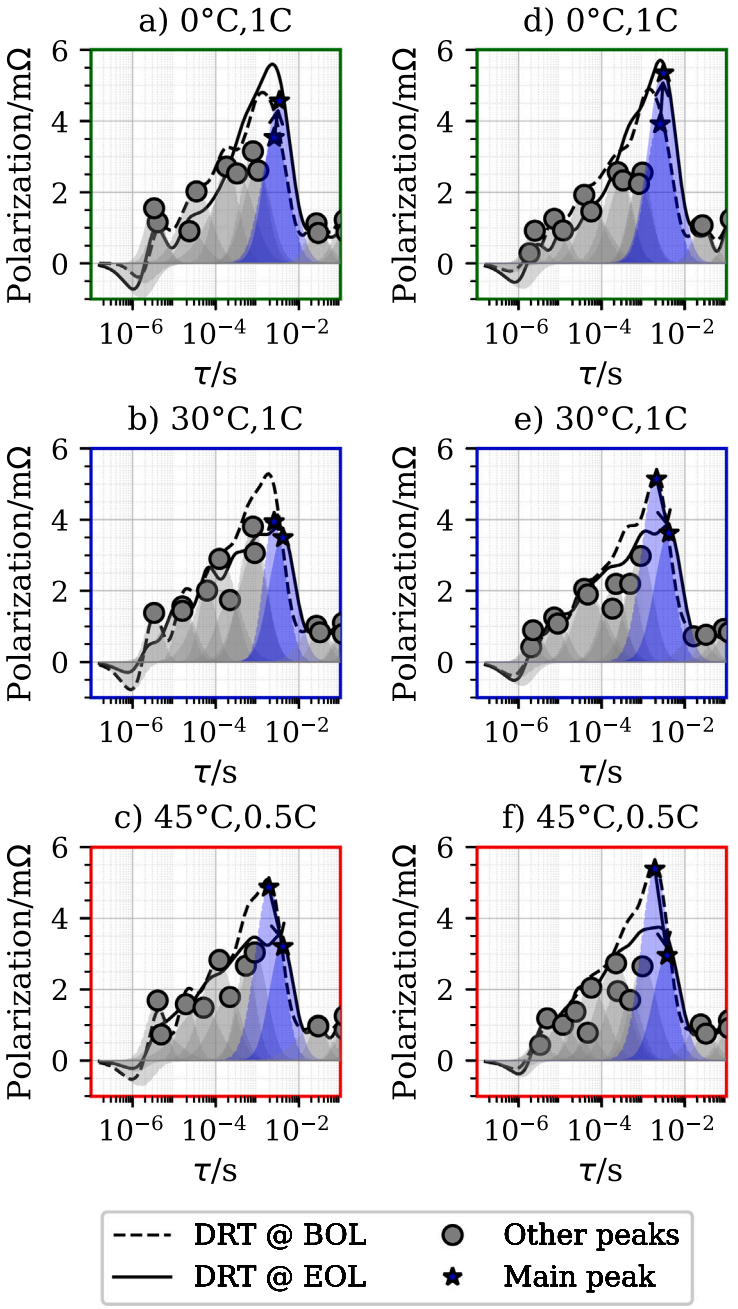

Fig. 10. Comparison of the evolution of the main peak of distribution function for two cells that each belong to the degradation pathways that were identified using PIS II. The main peak is highlighted in blue and the change from BOL (dashed) to EOL (solid) is indicated by an arrow. (a,d) Degradation pathway 1, (b, e) Degradation pathway 2, and (c, f) Degradation pathway 3. (a–c) Cell 1 and (d–f) Cell 2.

LAM_{PE} (~2%). Therefore, the validation experiments in general support our proposed methodology, which enables to identify different aging pathways from aging data using degradation modes. It should be noted that the degradation mechanisms that were discussed as possible causes for the different pathways are based on observed trends and are more indicative than definitive.

4.5. Design of PD II tests

A PD II test usually consists of a sequence of operating conditions that repeat until the cell reaches its EOL. Apart from these operating conditions the definition of EOL and the SFS also needs to be selected based on test requirements. The number of sequences of length r that can be formed from the number of possible stress conditions N is given by $\frac{N!}{(N-r)!}$. For example, from the 24 stress conditions tested in this work, the number of sequences of length 2 that can be formed is 552 and number of sequences of length 3 that can be formed is 12 144. In this section, the process of designing PD II tests is shown by using the cell and the SFS used in this study as an example.

As a first step, instead of arbitrarily selecting a value of $N < 24$ to reduce the experimental workload, the decision can be guided by the clustering framework described in this work. Fig. 11a shows the SFS, where the regions that trigger a specific degradation pathway are shaded with the corresponding color as determined from PIS II. These regions can be regarded as sets of operating conditions that are likely to activate distinct degradation mechanisms. Accordingly, the number of possible stress conditions N can be reduced from 24 to 3. From each

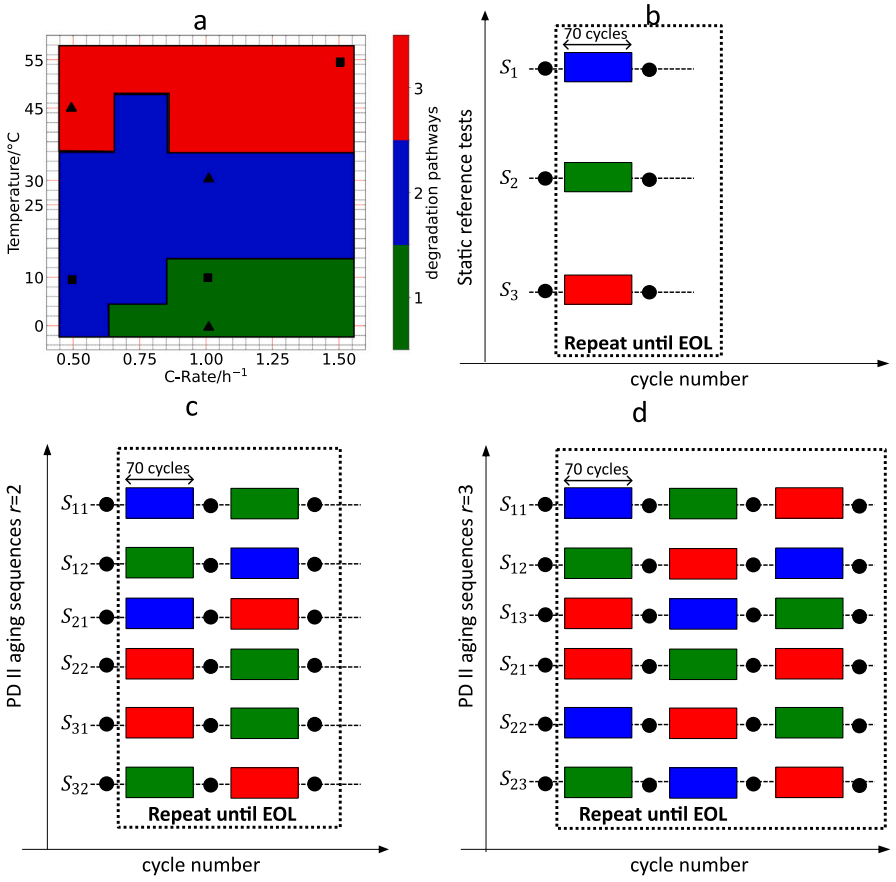

Fig. 11. Development of PD II tests using the degradation pathways identified from PIS II. (a) SFS with the center of the clusters identified in PIS II marked by black squares and points farthest away from cluster centers marked by black triangles. (b) Reference static aging tests at the 3 representative points, (c) Possible sequences of length 2 (d) Possible sequences of length 3.

region, a single point can be selected to represent the aging behavior associated with that pathway.

In this example, the centers of the three clusters could be identified in PIS II are mapped onto the SFS and marked by black squares. These three points serve as representative stress conditions for the respective degradation pathways. The point in the green region, from hereon referred to only as G corresponds to 10 °C, 1 C, the point in the blue region, from hereon referred to only as B corresponds to 10 °C, 0.5 C, and the point in the red region, from hereon referred to only as R corresponds to 55 °C, 1.5 C. In total, there can be 6 sequences of length 2 and 6 sequences of length 3 that can be formed from the three chosen conditions R, G, and B.

A practical PD II test protocol built using sequences of length 2 is shown in Fig. 11b and of length 3 is shown in Fig. 11c. The x-axis of the figure can represent either time or cycle number. Each of the black circles in the figure represent the RPT described in Section 2.3, each rectangle represents the aging protocol described in Section 2.4, where the color corresponds to the conditions R,G, and B. Additionally, it is recommended that static aging tests are also conducted at R, G, and B conditions as shown in Fig. 11d so that the trajectory of the cells aged under these conditions can be tracked in the PIS II and compared with the dynamic measurements. In this example, we propose that each aging block in the protocols shown in the figure be repeated for 70 cycles and the overall aging test be repeated until a specified EOL criteria such as 70% of the capacity of the cell at BOL is reached.

It should be noted that the example described here is just one way of building a PD II test using the framework described in the study. Firstly, instead of choosing the centers of the clusters found in PIS II as the representative point of the degradation pathway, points in the cluster that lie farthest from the centers could also be chosen as the points. These points are marked by a triangle in Fig. 11a. Secondly, in the example, when building PD II tests, the aim was to ensure the cell spends equal amount of time in each of the aging conditions R, G, and B. An another approach could be to modify the time spent by cell in each of the conditions such that they undergo approximately similar Λ_{Q_0}. Finally, the number of sequences that need to be tested could be further reduced to 3, if it is assumed that, under long-term cyclic repetition, a R-B sequence is equivalent to a B-R sequence, as the two differ only by a shift.

Therefore, a general guideline for defining PD II tests can be defined in the following way.

1. Use PIS II to identify distinct degradation pathways and map them onto the SFS.
2. Reduce the number of possible stress conditions N by selecting representative points from each pathway (e.g., cluster centers or points in a cluster that are farthest away from other centers).
3. Define the PD II protocol by choosing:
   - the sequence length r,
   - the number of sequences to test (accounting for equivalence of shifted sequences if desired),
   - and the number of cycles (or time) per aging block.
4. Insert RPTs and repeat the aging until the chosen EOL criterion (e.g., 70% capacity fade) is reached.

5. Conduct complementary static aging tests at the representative points to track reference degradation trajectories.
6. The duration of each operating condition within a sequence can either be equal or chosen such that it leads to similar change to a DM such as capacity fade.

5. Conclusion

In this study, *k*-means clustering, an unsupervised learning algorithm, is applied to analyze degradation metrics derived from aging tests on 48 commercial lithium-ion batteries cycled at six temperatures and four C-rates. Relative changes in these metrics, extracted from check-up cycles, are used to construct two PISs (PIS I and II), based on capacity fade and pulse resistance, and on degradation modes, respectively. Clustering is performed in each space, and cluster quality is assessed using SIL, DBI, and CHI. The resulting clusters are then mapped onto the SFS (temperature and C-rate) to identify stress conditions that give rise to distinct degradation pathways.

Both SIL and DBI chose 2 as the optimal number of clusters for PIS I consistently. Clustering the points in PIS I with 2 predefined cluster leads to the highest SIL of 0.72, lowest DBI of 0.35, and CHI of 88.60. When this cluster is mapped to the SFS, it reveals a distinct region that appears at a C-rate greater than 1 C for 10 °C and at a C-rate greater than 0.75 C for 0 °C. The other continuous region extends from low C-rates at low temperatures (0.5 C and 0 °C) to the higher temperatures, indicating that not enough information is available in the PIS to divide this region more. Clustering the points in PIS I with 3 predefined clusters, leads to a silhouette score of 0.63, DBI of 0.57, and CHI of 96.70. When these clusters are mapped to the SFS, they form three regions that could possibly trigger different degradation pathways. However, the two regions at lower temperatures effectively cut across each other. Therefore, the identified regions in the SFS that are not contiguous indicates that they represent the same pathway as the neighbor but at an earlier stage of degradation or it could mean the choice of the PIS is not sufficient to give a meaningful identification of aging pathways.

All of the metrics chose 3 as the optimal number of clusters for PIS II consistently. Clustering the points in PIS II with 3 predefined cluster leads to a silhouette score of 0.56, lowest DBI of 0.56, and highest CHI of 37.65. When this cluster is mapped to the SFS, it reveals a distinct region that appears at a C-rate greater than 1 C for 10 °C and at a C-rate greater than 0.75 C for 0 °C, similar to PIS I. The second region appears between 0.5 C and 0 °C and goes up to 30 °C, with one point located at 0.75 C and 45 °C. The third region appears at temperatures greater than 45 °C for all C-rates (except 0.75 C and 45 °C). By using the degradation modes that contain information about the degradation of individual electrodes, more physically meaningful identification of degradation pathways can be achieved. PIS II was also clustered with 4 predefined clusters and it leads to a silhouette score of 0.52, DBI of 0.49, and CHI of 31.12. This leads to the same identified degradation pathways as earlier, except that the cell at 0 °C and 1 C is considered to be belonging to a new degradation pathway. This could either be an indicator that this cell has the same degradation pathways as its neighbor, except that it has degraded more. But it is possibly also the starting point of another degradation pathway that might appear if the cells were aged at even lower temperatures.

Microscope analysis of the anode of individual cells in these three identified pathways (pathway 1–3) and a reference uncycled electrode revealed noticeable differences. The cell from the uncycled electrode looked mostly pristine except for some dark spots that looked similar in morphology to the electrode. The cell from pathway 1 (low temperatures,high C-rates) showed signs of plated lithium covering the anode surface and blocking the pores and additionally blackened spots in the electrodes, which could indicate possibly inactive regions of the electrode that led to LAMne. The cell from pathway 3, showed a relatively homogeneous electrode with some brownish deposits that could be some kind of electrolyte decomposition product. The cell in pathway 2, looked more homogeneous than the cell in pathway 1, but still showed some signs of having some deposits in the form of lines that could still be plating. They also showed the brown spots found for the cell in pathway 3. These differences could also be quantified by comparing the histograms of the overall pixel intensity distributions of the electrodes from the different pathways with the uncycled electrode.

DRT analysis of these cells showed that the cell from pathway 1 had a different polarization behavior in comparison to the cell in pathway 2 and 3, as its overall polarization contribution increased with aging. The cells from pathway 2 and 3 show differences that cannot be interpreted without a more detailed EIS study conducted on the cell. Cell from pathway 3 showed more reduction of polarization and slow down of the time constants of the polarization peaks with aging as compared to the cell from pathway 1.

In summary, the *k*-means algorithm has the high potential to uncover further insights from aging data to qualitatively distinguish degradation pathways. However, the choice of the PIS impacts the identified pathways, and this can be verified by ensuring that the clusters formed in the PIS also form continuous regions in the SFS. Future work should analyze more features of the aging data, such as NFRA and perform a deeper analysis of DRT to understand the impact of aging on different peaks. In addition, electrode images could also be used as features for the clustering process.

CRediT authorship contribution statement

S. Ramasubramanian: Writing – review & editing, Writing – original draft, Visualization, Validation, Software, Methodology, Investigation, Formal analysis, Data curation. **C. Plank:** Writing – review & editing, Writing – original draft, Validation, Software, Resources, Investigation, Formal analysis. **M.A. Danzer:** Writing – review & editing, Validation, Supervision, Resources, Funding acquisition. **F. Röder:** Writing – review & editing, Writing – original draft, Validation, Supervision, Resources, Project administration, Funding acquisition, Conceptualization.

Declaration of Generative AI and AI-assisted technologies in the writing process

During the preparation of this work the author(s) used ChatGPT and DeepL Write in order to shorten and/or rewrite some paragraphs to improve readability. After using this tool/service, the author(s) reviewed and edited the content as needed and take(s) full responsibility for the content of the publication.

Declaration of competing interest

The authors declare that they have no known competing financial interests or personal relationships that could have appeared to influence the work reported in this paper.

Acknowledgments

The authors would like to express their sincere gratitude to the European Union for supporting this work under the project 101103628 AccCellBaT. This work was also partially supported by the project "ILAB" (03XP0467) by the Federal Ministry of Education and Research in Germany (BMBF) and the project (527466263) by the German Research Foundation. The authors would like to thank Sophia Marie Sommer for the fruitful discussions on the topic. Additionally, the authors would like to thank Alexander Schmidt and Berk Oguz for assisting with opening the aged cells for postmortem analysis.

Data availability

The entire aging dataset including the EIS and NFRA data are available on Zenodo: https://doi.org/10.5281/zenodo.15755725.

References

[1] M. Yilmaz, P.T. Krein, Review of battery charger topologies, charging power levels, and infrastructure for plug-in electric and hybrid vehicles, IEEE Trans. Power Electron. 28 (5) (2012) 2151–2169.

[2] A. Tomaszewska, Z. Chu, X. Feng, S. O'kane, X. Liu, J. Chen, C. Ji, E. Endler, R. Li, L. Liu, et al., Lithium-ion battery fast charging: A review, ETransportation 1 (2019) 100011.

[3] Y. Zhou, X. Li, Vehicle to grid technology: A review, in: 2015 34th Chinese Control Conference, CCC, IEEE, 2015, pp. 9031–9036.

[4] J.S. Edge, S. O'Kane, R. Prosser, N.D. Kirkaldy, A.N. Patel, A. Hales, A. Ghosh, W. Ai, J. Chen, J. Yang, et al., Lithium ion battery degradation: what you need to know, Phys. Chem. Chem. Phys. 23 (14) (2021) 8200–8221.

[5] F. Röder, S. Ramasubramanian, A review and perspective on path dependency in batteries, Energy Technol. 10 (11) (2022) 2200627.

[6] L. Zhang, L. Wang, J. Zhang, Q. Wu, L. Jiang, Y. Shi, L. Lyu, G. Cai, Fault diagnosis of energy storage batteries based on dual driving of data and models, J. Energy Storage 112 (2025) 115485.

[7] Y. Zhang, Y. Zhang, B. Zheng, H. Cui, H. Qi, Statistical analysis for estimating the optimized battery capacity for roof-top PV energy system, Renew. Energy 242 (2025) 122491.

[8] S. Hansen, T. Rüther, M. Mennenga, C. Helbig, G. Ohnemüller, F. Vysoudil, C. Wolf, B. Rosemann, S. Pavón, A. Michaelis, et al., A structured approach for the compliance analysis of battery systems with regard to the new EU battery regulation, Resour. Conserv. Recycl. 209 (2024) 107752.

[9] W. Xia, S. Zheng, L. Qiu, H. Hu, Y. Chen, S. Wei, H. Zhou, Evolution of the innovation network of lithium-ion battery recycling technologies in China from the perspective of patents, Pol. J. Env. Stud. (2025).

[10] J. Schmalstieg, S. Käbitz, M. Ecker, D.U. Sauer, From accelerated aging tests to a lifetime prediction model: Analyzing lithium-ion batteries, in: 2013 World Electric Vehicle Symposium and Exhibition, EVS27, IEEE, 2013, pp. 1–12.

[11] J. de Hoog, J.-M. Timmermans, D. Ioan-Stroe, M. Swierczynski, J. Jaguemont, S. Goutam, N. Omar, J. Van Mierlo, P. Van Den Bossche, Combined cycling and calendar capacity fade modeling of a Nickel-Manganese-Cobalt Oxide cell with real-life profile validation, Appl. Energy 200 (2017) 47–61.

[12] L. Wildfeuer, A. Karger, D. Aygül, N. Wassiliadis, A. Jossen, M. Lienkamp, Experimental degradation study of a commercial lithium-ion battery, J. Power Sources 560 (2023) 232498.

[13] N. Kirkaldy, M.A. Samieian, G.J. Offer, M. Marinescu, Y. Patel, Lithium-ion battery degradation: Comprehensive cycle ageing data and analysis for commercial 21700 cells, J. Power Sources 603 (2024) 234185.

[14] A. Smith, J.C. Burns, X. Zhao, D. Xiong, J. Dahn, A high precision coulometry study of the SEI growth in Li/graphite cells, J. Electrochem. Soc. 158 (5) (2011) A447.

[15] L. Ellis, J. Allen, I. Hill, J. Dahn, High-precision coulometry studies of the impact of temperature and time on SEI formation in Li-ion cells, J. Electrochem. Soc. 165 (7) (2018) A1529.

[16] J. Christensen, J. Newman, A mathematical model of stress generation and fracture in lithium manganese oxide, J. Electrochem. Soc. 153 (6) (2006) A1019.

[17] I.D. Campbell, M. Marzook, M. Marinescu, G.J. Offer, How observable is lithium plating? Differential voltage analysis to identify and quantify lithium plating following fast charging of cold lithium-ion batteries, J. Electrochem. Soc. 166 (4) (2019) A725–A739.

[18] M. Ecker, P.S. Sabet, D.U. Sauer, Influence of operational condition on lithium plating for commercial lithium-ion batteries–Electrochemical experiments and post-mortem-analysis, Appl. Energy 206 (2017) 934–946.

[19] T. Raj, A.A. Wang, C.W. Monroe, D.A. Howey, Investigation of path-dependent degradation in lithium-ion batteries, Batter. Supercaps 3 (12) (2020) 1377–1385.

[20] M. Rogge, A. Jossen, Path-dependent ageing of lithium-ion batteries and implications on the ageing assessment of accelerated ageing tests, Batter. Supercaps 7 (1) (2024) e202300313.

[21] J. Liu, Y. Zhang, J. Bai, L. Zhou, Z. Wang, Influence of lithium plating on lithium-ion battery aging at high temperature, Electrochim. Acta 454 (2023) 142362.

[22] J. Liu, L. Zhou, Y. Zhang, J. Wang, Z. Wang, Aging behavior and mechanisms of lithium-ion battery under multi-aging path, J. Clean. Prod. 423 (2023) 138678.

[23] O. Gohar, M.Z. Khan, I. Bibi, N. Bashir, U. Tariq, M. Bakhtiar, M.R.A. Karim, F. Ali, M.B. Hanif, M. Motola, Nanomaterials for advanced energy applications: Recent advancements and future trends, Mater. Des. 241 (2024) 112930.

[24] H.G. Ali, K. Khan, M.B. Hanif, M.Z. Khan, I. Hussain, M.S. Javed, H.A. AL-bonsrulah, M. Mosiałek, M. Fichtner, M. Motola, Advancements in two-dimensional materials as anodes for lithium-ion batteries: Exploring composition-structure-property relationships emerging trends, and future perspective, J. Energy Storage 73 (2023) 108980.

[25] S. Friedrich, M. Bock, A. Jossen, Cycling aging in different state of charge windows in lithium-ion batteries with silicon-dominant anodes, J. Electrochem. Soc. 171 (10) (2024) 100503.

[26] T. Waldmann, A. Iturrondobeitia, M. Kasper, N. Ghanbari, F. Aguesse, E. Bekaert, L. Daniel, S. Genies, I.J. Gordon, M.W. Löble, et al., Post-mortem analysis of aged lithium-ion batteries: Disassembly methodology and physico-chemical analysis techniques, J. Electrochem. Soc. 163 (10) (2016) A2149.

[27] H. Xu, C. Han, W. Li, H. Li, X. Qiu, Quantification of lithium dendrite and solid electrolyte interphase (SEI) in lithium-ion batteries, J. Power Sources 529 (2022) 231219.

[28] Y. Peng, M. Ding, K. Zhang, H. Zhang, Y. Hu, Y. Lin, W. Hu, Y. Liao, S. Tang, J. Liang, et al., Quantitative analysis of the coupled mechanisms of lithium plating, SEI growth, and electrolyte decomposition in fast charging battery, ACS Energy Lett. 9 (12) (2024) 6022–6028.

[29] J. Schmitt, M. Schindler, A. Oberbauer, A. Jossen, Determination of degradation modes of lithium-ion batteries considering aging-induced changes in the half-cell open-circuit potential curve of silicon–graphite, J. Power Sources 532 (2022) 231296.

[30] G. Baure, A. Devie, M. Dubarry, Battery durability and reliability under electric utility grid operations: Path dependence of battery degradation, J. Electrochem. Soc. 166 (10) (2019) A1991.

[31] V. Sulzer, P. Mohtat, S. Pannala, J.B. Siegel, A.G. Stefanopoulou, Accelerated battery lifetime simulations using adaptive inter-cycle extrapolation algorithm, J. Electrochem. Soc. 168 (12) (2021) 120531.

[32] C.R. Birkl, M.R. Roberts, E. McTurk, P.G. Bruce, D.A. Howey, Degradation diagnostics for lithium ion cells, J. Power Sources 341 (2017) 373–386.

[33] A. Weng, J.B. Siegel, A. Stefanopoulou, Differential voltage analysis for battery manufacturing process control, Front. Energy Res. 11 (2023) 1087269.

[34] M. Dubarry, C. Truchot, B.Y. Liaw, Synthesize battery degradation modes via a diagnostic and prognostic model, J. Power Sources 219 (2012) 204–216.

[35] L. Zhou, L. Xie, J. Dai, A. Jain, G. Chen, Y. Zhao, Orthogonal test–based design and optimization of a li-ion battery thermal management system with a liquid-cooled reverse parallel structure and inlaid fins, Asia Pac. J. Chem. Eng. (2025) e70056.

[36] Y. Zhang, X. Li, L. Su, Z. Li, B.Y. Liaw, J. Zhang, Lithium plating detection and quantification in li-ion cells from degradation behaviors, Ecs Trans. 75 (23) (2017) 37.

[37] M. Bauer, C. Guenther, M. Kasper, M. Petzl, M.A. Danzer, Discrimination of degradation processes in lithium-ion cells based on the sensitivity of aging indicators towards capacity loss, J. Power Sources 283 (2015) 494–504.

[38] M. Heinrich, N. Wolff, N. Harting, V. Laue, F. Röder, S. Seitz, U. Krewer, Physico-chemical modeling of a lithium-ion battery: an ageing study with electrochemical impedance spectroscopy, Batter. Supercaps 2 (6) (2019) 530–540.

[39] E. Teliz, C.F. Zinola, V. Díaz, Identification and quantification of ageing mechanisms in li-ion batteries by electrochemical impedance spectroscopy, Electrochim. Acta 426 (2022) 140801.

[40] N. Wolff, N. Harting, M. Heinrich, U. Krewer, Nonlinear frequency response analysis on lithium-ion batteries: Process identification and differences between transient and steady-state behavior, Electrochim. Acta 298 (2019) 788–798.

[41] N. Harting, N. Wolff, U. Krewer, Identification of lithium plating in lithium-ion batteries using nonlinear frequency response analysis (NFRA), Electrochim. Acta 281 (2018) 378–385.

[42] B.-R. Chen, M.R. Kunz, T.R. Tanim, E.J. Dufek, A machine learning framework for early detection of lithium plating combining multiple physics-based electrochemical signatures, Cell Rep. Phys. Sci. 2 (3) (2021).

[43] S. Lloyd, Least squares quantization in PCM, IEEE Trans. Inform. Theory 28 (2) (1982) 129–137.

[44] S. Ramasubramanian, C. Plank, M. Danzer, F. Röder, Degradation path indicators for lithium-ion batteries, 2025.

[45] A. Barai, K. Uddin, W.D. Widanage, A. McGordon, P. Jennings, A study of the influence of measurement timescale on internal resistance characterisation methodologies for lithium-ion cells, Sci. Rep. 8 (1) (2018) 21.

[46] P. Keil, S.F. Schuster, J. Wilhelm, J. Travi, A. Hauser, R.C. Karl, A. Jossen, Calendar aging of lithium-ion batteries, J. Electrochem. Soc. 163 (9) (2016) A1872.

[47] O. Chaouachi, J.-M. Réty, S. Génies, M. Chandesris, Y. Bultel, Experimental and theoretical investigation of li-ion battery active materials properties: Application to a graphite/Ni0. 6Mn0. 2Co0. 2o2 system, Electrochim. Acta 366 (2021) 137428.

[48] A. Wang, S. O'Kane, F.B. Planella, J. Le Houx, K. O'Regan, M. Zyskin, J. Edge, C. Monroe, S. Cooper, D.A. Howey, et al., Review of parameterisation and a novel database (LiionDB) for continuum li-ion battery models, Prog. Energy 4 (3) (2022) 032004.

[49] C. Plank, T. Rüther, M.A. Danzer, Detection of non-linearity and non-stationarity in impedance spectra using an extended kramers-kronig test without overfitting, in: 2022 International Workshop on Impedance Spectroscopy, IWIS, IEEE, 2022, pp. 1–6.

[50] C. Plank, T. Rüther, L. Jahn, M. Schamel, J.P. Schmidt, F. Ciucci, M.A. Danzer, A review on the distribution of relaxation times analysis: A powerful tool for process identification of electrochemical systems, J. Power Sources 594 (2024) 233845.

[51] C. Schiller, F. Richter, E. Gülzow, N. Wagner, Validation and evaluation of electrochemical impedance spectra of systems with states that change with time, Phys. Chem. Chem. Phys. 3 (3) (2001) 374–378.
[52] C. Plank, T.G. Bergmann, N. Schlüter, M.A. Danzer, Distribution of relaxation times analysis for impedance spectra containing resistive-inductive characteristics: Part I. Deconvolution methods, J. Electrochem. Soc. 172 (6) (2025) 060514.
[53] M.A. Danzer, Generalized distribution of relaxation times analysis for the characterization of impedance spectra, Batteries 5 (3) (2019) 53.
[54] T. Paul, P. Chi, P.M. Wu, M. Wu, Computation of distribution of relaxation times by Tikhonov regularization for li ion batteries: usage of L-curve method, Sci. Rep. 11 (1) (2021) 12624.
[55] M. Hahn, S. Schindler, L.-C. Triebs, M.A. Danzer, Optimized process parameters for a reproducible distribution of relaxation times analysis of electrochemical systems, Batteries 5 (2) (2019) 43.
[56] F.N. Fritsch, J. Butland, A method for constructing local monotone piecewise cubic interpolants, SIAM J. Sci. Stat. Comput. 5 (2) (1984) 300–304.
[57] T. Baumhöfer, M. Brühl, S. Rothgang, D.U. Sauer, Production caused variation in capacity aging trend and correlation to initial cell performance, J. Power Sources 247 (2014) 332–338.
[58] P.J. Rousseeuw, Silhouettes: a graphical aid to the interpretation and validation of cluster analysis, J. Comput. Appl. Math. 20 (1987) 53–65.
[59] M.F.A.M. Ali, M.A.F. Muhalith, M.S.F. Sahran, Z.Q. Zubli, S.N.K. Kamarudin, S.A. Rahman, Clustering in game analysis on FIFA22 official players data, in: 2022 3rd International Conference on Artificial Intelligence and Data Sciences, AiDAS, IEEE, 2022, pp. 49–54.
[60] S. Noei, H. Li, S. Georgiou, Y. Zou, An empirical study of refactoring rhythms and tactics in the software development process, IEEE Trans. Softw. Eng. 49 (12) (2023) 5103–5119.
[61] B.M. Tijms, E.M. Vromen, O. Mjaavatten, H. Holstege, L.M. Reus, S. van der Lee, K.E. Wesenhagen, L. Lorenzini, L. Vermunt, V. Venkatraghavan, et al., Cerebrospinal fluid proteomics in patients with Alzheimer's disease reveals five molecular subtypes with distinct genetic risk profiles, Nat. Aging 4 (1) (2024) 33–47.
[62] D.L. Davies, D.W. Bouldin, A cluster separation measure, IEEE Trans. Pattern Anal. Mach. Intell. (2) (2009) 224–227.
[63] T. Caliński, J. Harabasz, A dendrite method for cluster analysis, Comm. Statist. Theory Methods 3 (1) (1974) 1–27.
[64] D. Arthur, S. Vassilvitskii, K-Means++: The Advantages of Careful Seeding, Tech. Rep., Stanford, 2006.
[65] T. Waldmann, M. Wilka, M. Kasper, M. Fleischhammer, M. Wohlfahrt-Mehrens, Temperature dependent ageing mechanisms in lithium-ion batteries–A post-mortem study, J. Power Sources 262 (2014) 129–135.
[66] M. Bozorgchenani, G. Kucinskis, M. Wohlfahrt-Mehrens, T. Waldmann, Experimental confirmation of C-rate dependent minima shifts in Arrhenius plots of li-ion battery aging, J. Electrochem. Soc. 169 (3) (2022) 030509.
[67] G. Kucinskis, M. Bozorgchenani, M. Feinauer, M. Kasper, M. Wohlfahrt-Mehrens, T. Waldmann, Arrhenius plots for li-ion battery ageing as a function of temperature, C-rate, and ageing state–An experimental study, J. Power Sources 549 (2022) 232129.
[68] M. Feinauer, M. Wohlfahrt-Mehrens, M. Hölzle, T. Waldmann, Temperature-driven path dependence in li-ion battery cyclic aging, J. Power Sources 594 (2024) 233948.
[69] M. Petzl, M.A. Danzer, Nondestructive detection, characterization, and quantification of lithium plating in commercial lithium-ion batteries, J. Power Sources 254 (2014) 80–87.
[70] H.-G. Schweiger, O. Obeidi, O. Komesker, A. Raschke, M. Schiemann, C. Zehner, M. Gehnen, M. Keller, P. Birke, Comparison of several methods for determining the internal resistance of lithium ion cells, Sensors 10 (6) (2010) 5604–5625.
[71] W. Waag, S. Käbitz, D.U. Sauer, Experimental investigation of the lithium-ion battery impedance characteristic at various conditions and aging states and its influence on the application, Appl. Energy 102 (2013) 885–897.
[72] S.P. Rangarajan, Y. Barsukov, P.P. Mukherjee, In operando signature and quantification of lithium plating, J. Mater. Chem. 7 (36) (2019) 20683–20695.
[73] P. Gasper, N. Sunderlin, N. Dunlap, P. Walker, D.P. Finegan, K. Smith, F. Thakkar, Lithium loss, resistance growth, electrode expansion, gas evolution, and li plating: Analyzing performance and failure of commercial large-format NMC-Gr lithium-ion pouch cells, J. Power Sources 604 (2024) 234494.
[74] K.W. Knehr, T. Hodson, C. Bommier, G. Davies, A. Kim, D.A. Steingart, Understanding full-cell evolution and non-chemical electrode crosstalk of li-ion batteries, Joule 2 (6) (2018) 1146–1159.
[75] B. Stiaszny, J.C. Ziegler, E.E. Krauß, J.P. Schmidt, E. Ivers-Tiffée, Electrochemical characterization and post-mortem analysis of aged LiMn2O4–Li (Ni0. 5Mn0. 3Co0. 2) O2/graphite lithium ion batteries. Part I: Cycle aging, J. Power Sources 251 (2014) 439–450.
[76] J. Zhou, P. Notten, Studies on the degradation of li-ion batteries by the use of microreference electrodes, J. Power Sources 177 (2) (2008) 553–560.
[77] F. Katzer, P. Mößle, M. Schamel, M.A. Danzer, Adaptive fast charging control using impedance-based detection of lithium deposition, J. Power Sources 555 (2023) 232354.
[78] L. Bläubaum, F. Röder, C. Nowak, H.S. Chan, A. Kwade, U. Krewer, Impact of particle size distribution on performance of lithium-ion batteries, ChemElectroChem 7 (23) (2020) 4755–4766.
[79] W. Wu, W. Wu, X. Qiu, S. Wang, Low-temperature reversible capacity loss and aging mechanism in lithium-ion batteries for different discharge profiles, Int. J. Energy Res. 43 (1) (2019) 243–253.
[80] U.R. Koleti, A. Rajan, C. Tan, S. Moharana, T.Q. Dinh, J. Marco, A study on the influence of lithium plating on battery degradation, Energies 13 (13) (2020) 3458.
[81] C. Pastor-Fernández, K. Uddin, G.H. Chouchelamane, W.D. Widanage, J. Marco, A comparison between electrochemical impedance spectroscopy and incremental capacity-differential voltage as li-ion diagnostic techniques to identify and quantify the effects of degradation modes within battery management systems, J. Power Sources 360 (2017) 301–318.
[82] M. Dubarry, A. Pearson, K. Pringle, Y. Shekibi, S. Pas, Impact of temperature and depth of discharge on commercial Nickel manganese oxide and lithium iron phosphate batteries after three years of aging, Batteries 11 (7) (2025) 239.
[83] T. Rüther, W. Hileman, G.L. Plett, M.S. Trimboli, M.A.A. Danzer, Demystifying the distribution of relaxation times: A simulation-based investigation into the limits and possibilities of interpretation for lithium-ion batteries, J. Electrochem. Soc. (2024).
[84] P. Iurilli, C. Brivio, V. Wood, Detection of lithium-ion cells' degradation through deconvolution of electrochemical impedance spectroscopy with distribution of relaxation time, Energy Technol. 10 (10) (2022) 2200547.
[85] T.L. Kirk, A. Lewis-Douglas, D. Howey, C.P. Please, S.J. Chapman, Nonlinear electrochemical impedance spectroscopy for lithium-ion battery model parameterization, J. Electrochem. Soc. 170 (1) (2023) 010514.
[86] N. Wolff, N. Harting, M. Heinrich, F. Röder, U. Krewer, Nonlinear frequency response analysis on lithium-ion batteries: a model-based assessment, Electrochim. Acta 260 (2018) 614–622.
[87] W. Shen, N. Wang, J. Zhang, F. Wang, G. Zhang, Heat generation and degradation mechanism of lithium-ion batteries during high-temperature aging, ACS Omega 7 (49) (2022) 44733–44742.
[88] M. Dubarry, G. Baure, D. Anseán, Perspective on state-of-health determination in lithium-ion batteries, J. Electrochem. Energy Convers. Storage 17 (4) (2020) 044701.
[89] F. Ringbeck, C. Rahe, G. Fuchs, D.U. Sauer, Identification of lithium plating in lithium-ion batteries by electrical and optical methods, J. Electrochem. Soc. 167 (9) (2020) 090536.
[90] M. Lewerenz, A. Warnecke, D.U. Sauer, Post-mortem analysis on LiFePO4| graphite cells describing the evolution & composition of covering layer on anode and their impact on cell performance, J. Power Sources 369 (2017) 122–132.
[91] A.M. Syed, A. Jodlbauer, M. Wilkening, H. Wiltsche, J.V. Ecker, C. Ellersdorfer, G. Gstrein, I. Hanzu, Post-mortem identification of lithium plating in high energy automotive batteries, Sustain. Energy Fuels (2025).
[92] P. Bai, J. Li, F.R. Brushett, M.Z. Bazant, Transition of lithium growth mechanisms in liquid electrolytes, Energy Environ. Sci. 9 (10) (2016) 3221–3229.
[93] T. Rüther, W. Hileman, G. Plett, M. Trimboli, M. Danzer, Demystifying the distribution of relaxation times: A simulation-based investigation into the limits and possibilities of interpretation for lithium-ion batteries, J. Electrochem. Soc. 171 (2024) http://dx.doi.org/10.1149/1945-7111/ad4fe5.